
Phase diagram of training dynamics in deep neural networks: effect of learning rate, depth, and width

Dayal Singh Kalra^{1,2} Maissam Barkeshli^{3,2,4}

Abstract

We systematically analyze optimization dynamics in deep neural networks (DNNs) trained with stochastic gradient descent (SGD) over long time scales and study the effect of learning rate, depth, and width of the neural network. By analyzing the maximum eigenvalue λ_t^H of the Hessian of the loss, which is a measure of sharpness of the loss landscape, we find that the dynamics can show four distinct regimes: (i) an early time transient regime, (ii) an intermediate saturation regime, (iii) a progressive sharpening regime, and finally (iv) a late time “edge of stability” regime. The early and intermediate regimes (i) and (ii) exhibit a rich phase diagram depending on learning rate $\eta \equiv c/\lambda_0^H$, depth d , and width w . We identify several critical values of c which separate qualitatively distinct phenomena in the early time dynamics of training loss and sharpness, and extract their dependence on d/w . Our results have implications for how to scale the learning rate with DNN depth and width in order to remain in the same phase of learning.

1. Introduction

The optimization dynamics of deep neural networks (DNNs) is a rich problem that is of fundamental and practical interest. Seemingly small changes to the hyperparameters can dramatically alter the effectiveness of training and even lead to training failures. Basic questions about how to choose learning rates and their effect on generalization error and training speed remain intensely studied research problems.

¹Institute for Physical Science and Technology, University of Maryland, College Park, Maryland 20742, USA ²Condensed Matter Theory Center, University of Maryland, College Park, Maryland 20742, USA ³Department of Physics, University of Maryland, College Park, Maryland 20742, USA ⁴Joint Quantum Institute, University of Maryland, College Park, Maryland 20742, USA. Correspondence to: Dayal Singh Kalra <dayal@umd.edu>, Maissam Barkeshli <maissam@umd.edu>.

Classical intuition from convex optimization has led to the oft-made suggestion that in stochastic gradient descent (SGD), the learning rate η should satisfy $\eta < 2/\lambda^H$, where λ^H is the maximum eigenvalue of the Hessian H of the loss, in order to ensure that the network reaches a minimum. However several recent studies have suggested that it is both possible and potentially preferable to have the learning rate *early in training* reach $\eta > 2/\lambda^H$ (Wu et al., 2018; Lewkowycz et al., 2020; Zhu et al., 2022). The idea is that such a choice will induce a temporary training instability, causing the network to ‘catapult’ out of a local basin into a flatter one with lower λ^H where training stabilizes. Indeed, during the early training phase, the local curvature of the loss landscape changes rapidly (Keskar et al., 2016; Achille et al., 2017; Jastrzebski et al., 2018; Fort & Ganguli, 2019), and the learning rate plays a crucial role in determining the convergence basin (Jastrzebski et al., 2018). Flatter basins are believed to be preferable because they potentially lead to lower generalization error (Hochreiter & Schmidhuber, 1994; 1997; Keskar et al., 2016; Dziugaite & Roy, 2017; Jiang et al., 2019; Foret et al., 2020) and allow larger learning rates leading to potentially faster training.

From a different perspective, the major theme of deep learning is that it is beneficial to increase the model size as much as possible. This has come into sharp focus with the discovery of scaling laws that show power law improvement in generalization error with model and dataset size (Kaplan et al., 2020). This raises the fundamental question of how one can scale DNNs to arbitrarily large sizes while maintaining the ability to learn; in particular, how should initialization and optimization hyperparameters be chosen to maintain a similar quality of learning as the architecture size is taken to infinity (Jacot et al., 2018; Lee et al., 2018; 2019; Dyer & Gur-Ari, 2020; Yang & Hu, 2021; Roberts et al., 2022; Yang et al., 2022; Yaida, 2022)?

Motivated by these ideas, we perform a systematic analysis of the training dynamics of SGD for DNNs as learning rate, depth, and width are tuned, across a variety of architectures and datasets. We monitor both the loss and sharpness (λ^H) trajectories out to late times, observing a number of qualitatively distinct phenomena summarized below.

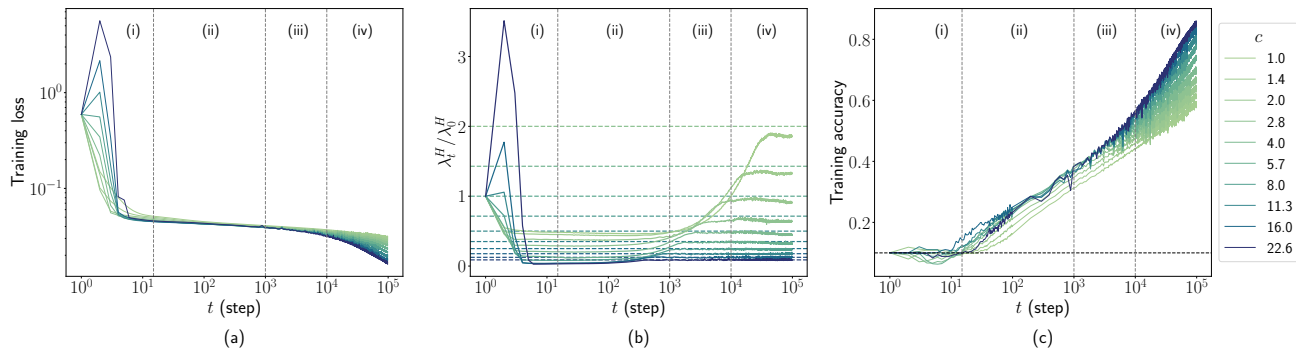


Figure 1. Full training trajectories of the (a) training loss, (b) sharpness, and (c) training accuracy of CNNs ($d = 5$ and $w = 512$) trained on CIFAR-10 with MSE loss using vanilla SGD with learning rates $\eta = c/\lambda_0^H$ and batch size $B = 512$. Vertical dashed lines approximately separate the different training regimes. Horizontal dashed lines in (b) denote the $2/\eta$ threshold for each learning rate. In Appendix G.1 we show the same trajectories with the time axis rescaled as ct .

1.1. Our contributions

We study SGD on fully connected networks (FCNs) with the same number of hidden units (width) in each layer, convolutional neural networks (CNNs) and ResNet architectures of varying width w and depth d with ReLU activation. For CNNs, the width corresponds to the number of channels. We parameterize FCNs in the Neural Tangent Parameterization (NTP) (Jacot et al., 2018) and CNNs and ResNets in Standard Parameterization (SP) (Sohl-Dickstein et al., 2020); other parameterizations, such as muP (Yang & Hu, 2021), can give different results. For further details, see Appendix A. We study both mean-squared error (MSE) and cross-entropy loss functions, and the datasets CIFAR-10, MNIST, Fashion-MNIST. The basic phenomena we report are reliably reproduced across these architectures and datasets. We use sharpness to refer to λ_t^H , the maximum eigenvalue of H at time-step t , and flatness refers to $1/\lambda_t^H$.

By monitoring the sharpness, we find four clearly separated, qualitatively distinct regimes throughout the entire span of the training trajectory. Fig. 1 shows an example from a CNN architecture. The four observed regimes are: (i) an early time transient regime, (ii) an intermediate saturation regime where the sharpness has lowered and remains relatively constant, (iii) a progressive sharpening regime, and finally (iv) a late time “edge of stability” regime where the sharpness saturates around $2/\eta$ (Cohen et al., 2021).

Next, we analyze the early transient and intermediate saturation regimes. For MSE loss, a clear picture emerges, and leads to a rich phase diagram, sketched in Figure 2, as learning rate, d , and w are tuned. Given the learning rate scaled as $\eta = c/\lambda_0^H$, we characterize four distinct behaviors in the training dynamics in the early transient regime (i):

1. **Sharpness reduction phase** ($c < c_{loss}$): Both the loss and the sharpness monotonically decrease during

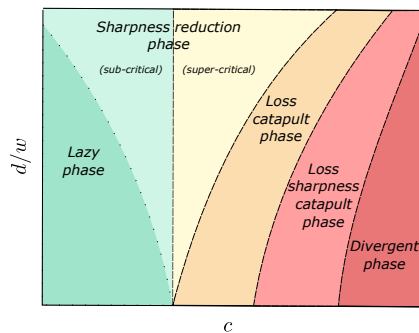


Figure 2. Sketched phase diagram of early training

early training. There is a particularly significant drop in sharpness in the regime $2 \approx c_{crit} < c < c_{loss}$, which motivates us to refer to learning rates lower than c_{crit} as sub-critical and larger than c_{crit} as super-critical. The regime $c_{crit} < c < c_{loss}$ opens up significantly with increasing d/w , which is a new result of this work.

2. **Loss catapult phase** ($c_{loss} < c < c_{sharp}$): The first few gradient steps take training to a flatter region but with a higher loss. Training eventually settles down in the flatter region as the loss starts to decrease again. The sharpness *monotonically decreases from initialization* in this early time transient regime.
3. **Loss and sharpness catapult phase** ($c_{sharp} < c < c_{max}$): In this regime *both the loss and sharpness* initially start to increase, effectively catapulting to a different point where loss and sharpness can start to decrease again. Training eventually exhibits a significant reduction in sharpness by the end of the early training. The report of a *loss and sharpness catapult* is also new to this work.
4. **Divergent phase** ($c > c_{max}$): The learning rate is too

large for training to converge and the loss diverges.

The critical values c_{loss} , c_{sharp} , c_{max} are random variables that depend on random initialization, SGD batch selection, and architecture. The averages of c_{loss} , c_{sharp} , c_{max} are shown in the phase diagrams and show strong systematic dependence on d/w .

We also analyze the linear connectivity of the loss landscape in the early transient regime and show that for a range of learning rates $c_{loss} < c < c_{barrier}$, no barriers exist from the initial state to the final point of the initial transient phase, even though training passes through regions with higher loss than initialization.

Next, we provide a quantitative analysis of the intermediate saturation regime. We find that sharpness during this time typically displays 3 distinct regimes as the learning rate is tuned, depicted in Fig. 6. By identifying an appropriate order parameter we can extract a sharp peak corresponding to $c_{crit} \approx 2/\lambda_0^H$. For $c \ll c_{crit}$, the network is effectively in a lazy training regime, with increasing fluctuations as d/w is increased.

Finally, we show that a single hidden layer linear network – the uw model – displays the same phenomena discussed above for the early regimes (i) and (ii), and we analyze the phase diagram in this minimal model.

1.2. Related works

A significant amount of research has identified various training regimes using diverse criteria, e.g., (Erhan et al., 2010; Achille et al., 2017; Fort et al., 2020; Jastrzebski et al., 2018; Frankle et al., 2020; Leclerc & Madry, 2020; Jastrzebski et al., 2020; Cohen et al., 2021; Iyer et al., 2022). Here we focus on studies that characterize training regimes with sharpness and learning rates.

Several studies have analyzed sharpness at different training times (Jastrzebski et al., 2018; Fort & Ganguli, 2019; Jastrzebski et al., 2020; Cohen et al., 2021; Iyer et al., 2022). (Cohen et al., 2021) studied sharpness at late training times and showed how *large-batch* gradient descent shows progressive sharpening followed by the edge of stability: For MSE loss, the sharpness increases until it reaches a maximum value just above $2/\eta$ and oscillates near it. This has motivated various theoretical studies (Damian et al., 2022; Agarwala et al., 2022; Arora et al., 2022). We add to this line of work by demonstrating a wide variety of architectures trained with SGD with relatively small batch sizes $B = 512$, $\approx 1\%$ of the full training set, that clearly show progressive sharpening and edge of stability phenomena.

(Jastrzebski et al., 2018) studied the entire training trajectory of sharpness in models trained with SGD and cross-entropy loss and found that sharpness increases during the early

stages of training, reaches a peak, and then decreases. In contrast, we find a sharpness-reduction phase, $c < c_{loss}$ which becomes more prominent with increasing d/w , where sharpness only decreases during early training; this also occurs in the catapult phase $c_{loss} < c < c_{sharp}$, during which the loss initially increases before decreasing. This discrepancy is likely due to different initialization and learning rate scaling in their work (Iyer et al., 2022).

(Jastrzebski et al., 2020) examined the effect of hyperparameters on sharpness at late training times. (Gilmer et al., 2021) studied the optimization dynamics of SGD with momentum using sharpness. (Leclerc & Madry, 2020) classify training into 2 different regimes using training loss, providing a significantly coarser description of training dynamics than provided here. (Iyer et al., 2022) studied the scaling of the maximum learning rate with d and w during early training in FCNs and its relationship with sharpness at initialization.

(Lewkowycz et al., 2020) analyzed the curvature during early training using the top eigenvalue of the neural tangent kernel (NTK) and demonstrated the existence of a new early training phase, which they dubbed the ‘‘catapult’’ phase, $2/\lambda_0^{NTK} < \eta < \eta_{max}$, in wide networks trained with MSE loss using SGD, in which training converges after an initial increase in training loss. The existence of this new training regime was further extended to quadratic models with large widths by (Zhu et al., 2022; Meltzer & Liu, 2023). Our work extends the above analysis by studying the combined effect of learning rate, depth, and width, demonstrating the opening of a sharpness-reduction phase, the refinement of the catapult phase into two phases depending on whether the sharpness also catapults, analyzing the phase boundaries as d/w is increased, analyzing linear mode connectivity in the catapult phase, and also examining different qualitative behaviors in the intermediate saturation regime (ii) mentioned above.

2. The four regimes of training

Figure 1 illustrates the training trajectories of a 5-layer deep ($d = 5$) CNN from the Myrtle family (Shankar et al., 2020), trained on the CIFAR-10 dataset using MSE loss. Each network layer has $w = 128$ channels. The networks were trained using SGD with various learning rates and a batch size of $B = 512$. These results indicate that the training dynamics can be divided into four distinct regimes based on training loss and sharpness:

- (i) **Early time transient:** ($0 < t < T_1$). Within a few (~ 10) training steps, training selects the convergence basin, which depends on the optimization hyperparameters. The loss and sharpness may drastically change, and training eventually settles down in a basin by the end of this short period.

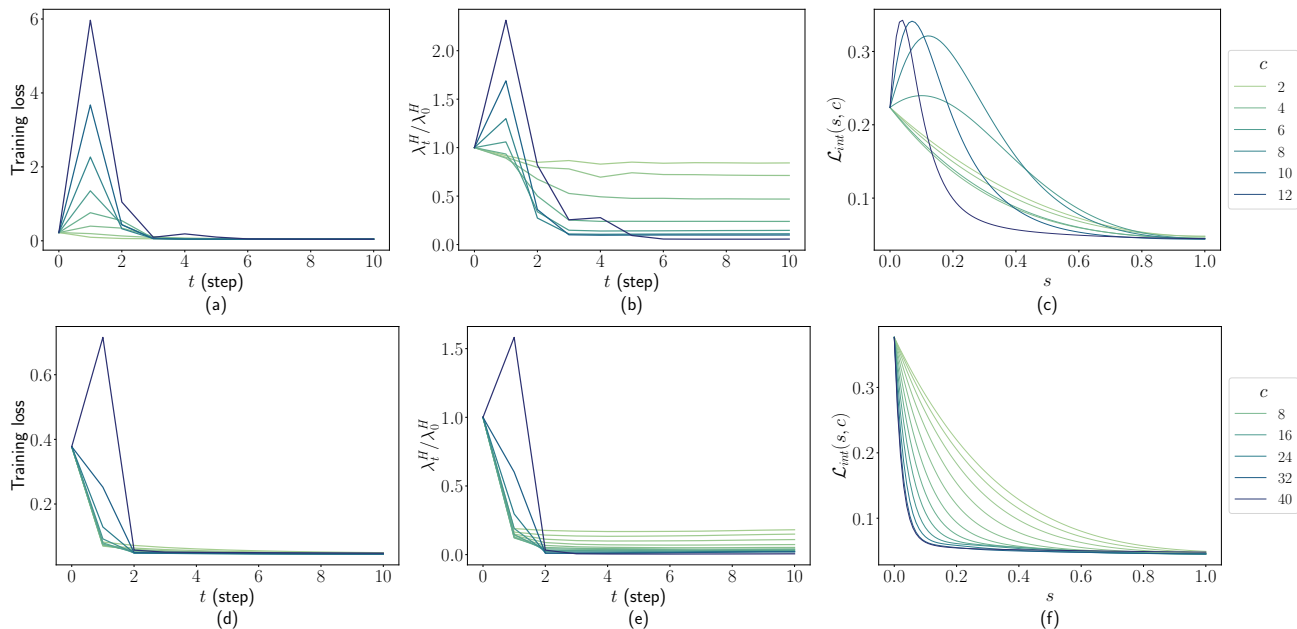


Figure 3. Early training dynamics of (a, b, c) a shallow ($d = 5, w = 512$) and (d, e, f) a deep CNN ($d = 10, w = 128$) trained on CIFAR-10 with MSE loss for $t = 10$ steps using SGD for various learning rates $\eta = c/\lambda_0^H$ and batch size $B = 512$. (a, d) training loss, (b, e) sharpness, and (c, f) interpolated loss between the initial and final parameters after 10 steps for the respective models. For the shallow CNN, $c_{loss} = 2.82, c_{sharp} = 5.65, c_{max} = 17.14$ and for the deep CNN, $c_{loss} = 36.75, c_{sharp} = 39.39, c_{max} = 48.50$.

- (ii) **Intermediate saturation:** ($T_1 < t < T_2$). The learning rate is small compared to sharpness, resulting in a slow transient period. The sharpness changes slowly until it reaches a tipping point T_2 , which marks this regime’s end.
- (iii) **Progressive sharpening:** ($T_2 < t < T_3$). The sharpness steadily rises until it reaches a maximum value $\approx 2/\eta$ (Jastrzebski et al., 2020; Cohen et al., 2021).
- (iv) **Late time:** ($T_3 < t$). Training dynamics show different phenomena depending on the loss and optimization parameters. For networks trained with MSE loss and large enough batch sizes, training enters a stable cycle in which sharpness oscillates around this maximum value, and the training loss fluctuates while decreasing overall. In comparison, sharpness may drop after reaching this maximum value for cross-entropy loss while remaining less than $2/\eta$.

We confirm the existence of the four training regimes across various architectures, datasets, and loss functions as demonstrated in Appendix G. Our results show that FCNs, CNNs, and ResNets, when trained on CIFAR-10, MNIST, and Fashion-MNIST datasets, using MSE and cross-entropy loss, exhibit all four training regimes. An exception to this observation is that FCNs did not exhibit the fourth regime (iv), even after training for 1000 epochs.

Note the log scale in Fig. 1 highlights the early regimes (i)

and (ii); in absolute terms these are much shorter in time than regimes (iii) and (iv).

3. Phase diagram of early transient regime

For wide enough networks trained with MSE loss using SGD, training converges into a flatter region after an initial increase in the training loss for learning rates $c > 2$ (Lewkowycz et al., 2020). Figure 3(a, b) shows the first 10 steps of the loss and sharpness trajectories of a shallow ($d = 5$ and $w = 512$) CNN trained on the CIFAR-10 dataset with MSE loss using SGD. For learning rates, $c \geq 2.82$, the loss catapults and training eventually converges into a flatter region, as measured by sharpness. Additionally, we observe that sharpness may also spike initially, similar to the training loss (see Figure 3 (b)). However, this initial spike in sharpness occurs at relatively higher learning rates ($c \geq 5.65$), which we will examine along with the loss catapult. We refer to this spike in sharpness as ‘sharpness catapult.’

An important consideration is the degree to which this phenomenon changes with network depth and width. Interestingly, we found that the training loss in deep networks on average catapults at much larger learning rates than $c = 2$. Figure 3(c, d) shows that for a deep ($d = 10, w = 128$) CNN, the loss and sharpness may catapult only near the maximum trainable learning rate. In this section, we characterize the properties of the early training dynamics of models with MSE loss. For cross-entropy loss, we found

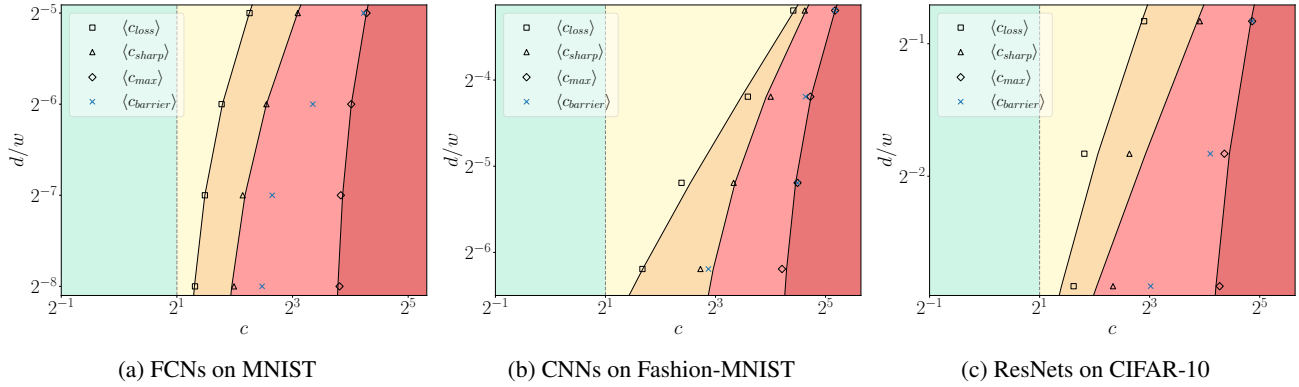


Figure 4. The phase diagrams of the early training of three different types of neural networks trained with MSE loss function using SGD. (a) FCNs ($d = 8$) trained on the MNIST dataset, (b) CNNs ($d = 7$) trained on the Fashion-MNIST dataset, (c) ResNet ($d = 18$) trained on the CIFAR-10 dataset (without batch normalization). Each data point in the figure represents an average of ten distinct initialization, and the solid lines represent a smooth curve fitted to the raw data points. The vertical dotted line shows $c = 2$ for comparison, and various colors are filled in between the various curves for better visualization. For experimental details and additional results for different depths, see Appendices A and C, respectively.

that the early time dynamics is more chaotic and it is unclear to what extent it can be separated into different phases.

3.1. Loss and sharpness catapult during early training

In this subsection, we characterize the effect of finite depth and width on the onset of the loss and sharpness catapult and training divergence. We begin by defining critical constants that correspond to the above phenomena.

Definition 3.1. ($c_{loss}, c_{sharp}, c_{max}$) For learning rate $\eta = c/\lambda_0^H$, let the training loss and sharpness at step t be denoted by $\mathcal{L}_t(c)$ and $\lambda_t^H(c)$. We define $c_{loss}(c_{sharp})$ as minimum learning rates constants such that the loss (sharpness) increases during the initial transient period

$$c_{loss} = \min_c \{c \mid \max_{t \in [1, T_1]} \mathcal{L}_t(c) > \mathcal{L}_0(c)\} \quad (1)$$

$$c_{sharp} = \min_c \{c \mid \max_{t \in [1, T_1]} \lambda_t^H(c) > \lambda_0^H(c)\}, \quad (2)$$

and c_{max} as the maximum learning rate constant such that the loss does not diverge during the initial transient period

$$c_{max} = \max_c \{c \mid \mathcal{L}_t(c) < K, \forall t \in [1, T_1]\}, \quad (3)$$

where K is a fixed large constant¹.

Note that the definition of c_{max} allows for more flexibility than previous studies (Iyer et al., 2022) in order to investigate a wider range of phenomena occurring near the maximum learning rate. Here, c_{loss} , c_{sharp} , and c_{max} are random variables that depend on the random initialization

¹We use $K = 10^5$ to estimate c_{max} . In all our experiments, $\mathcal{L}_0 = \mathcal{O}(1)$ (see Appendix A), which justifies the use of a fixed value.

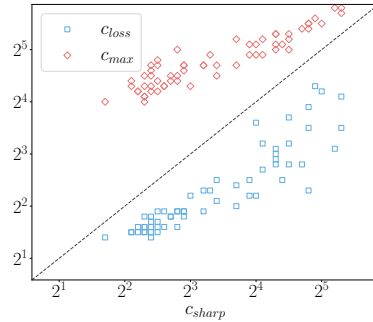


Figure 5. The relationship between critical constants for ResNets with $d \in \{18, 34\}$, $w \in \{32, 64, 128\}$, trained on the CIFAR-10 dataset. Each data point corresponds to a randomly initialized model. The dashed line represents the $y = x$ line. For experimental details and additional results, see Appendices A and D.

and the SGD batch sequence, and we denote the average over this randomness using $\langle \cdot \rangle$.

Figure 4 illustrates the phase diagram of early training for three different architectures trained on various datasets with MSE loss using SGD. These phase diagrams show how the averaged values $\langle c_{loss} \rangle$, $\langle c_{sharp} \rangle$, and $\langle c_{max} \rangle$ are affected by network depth and width when plotted in the subspace represented by the depth-to-width ratio (d/w). This choice is motivated by various studies that show how in FCNs, the ratio d/w controls the fluctuations (Hanin & Nica, 2019; Dyer & Gur-Ari, 2020; Roberts et al., 2022). The results show that the averaged values of all the critical constants increase significantly with d/w (note the log scale). At small values of d/w , the loss starts to catapult at $c \approx 2$. As d/w increases, $\langle c_{loss} \rangle$ increases and eventually converges to $\langle c_{max} \rangle$ at large d/w . By comparison, sharpness starts to

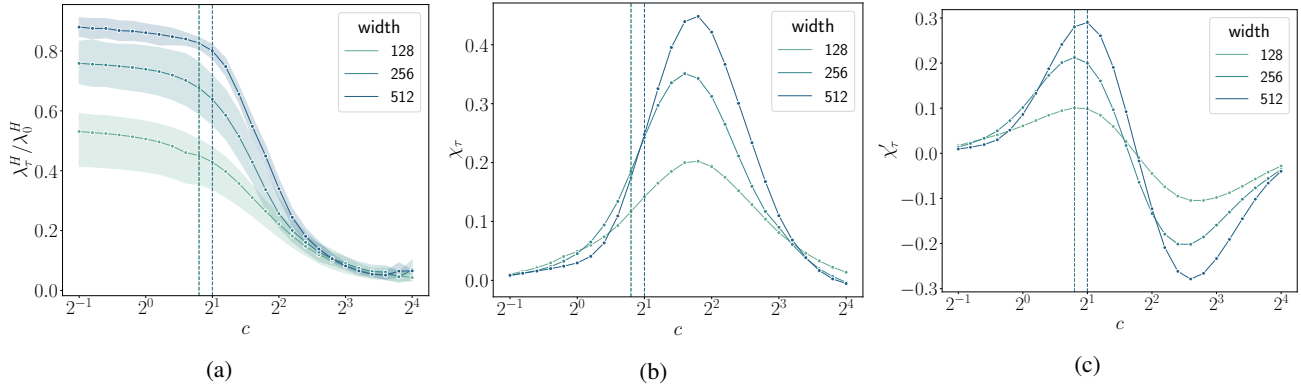


Figure 6. (a) Normalized sharpness measured at $c\tau = 200$ against the learning rate constant for 7-layer CNNs trained on the CIFAR-10 dataset, with varying widths. Each data point is an average over 5 initializations, where the shaded region depicts the standard deviation around the mean trend. (b, c) Smooth estimations of the first two derivatives, χ_τ and χ'_τ , of the averaged normalized sharpness wrt the learning rate constant. The vertical lines denote c_{crit} estimated using the maximum of χ'_τ . For smoothing details, see Appendix E.2.

catapult at relatively large learning rates at small d/w , with $\langle c_{sharp} \rangle$ continuing to increase with d/w while remaining between $\langle c_{loss} \rangle$ and $\langle c_{max} \rangle$. Moreover, although $\langle c_{max} \rangle$ increases with d/w , the bare learning rate $\eta_{max} \equiv c_{max} / \lambda_0^H$ decreases on average with d/w .

While we plotted the averaged quantities $\langle c_{loss} \rangle$, $\langle c_{sharp} \rangle$, $\langle c_{max} \rangle$, we have observed that their variance also increases significantly with d/w ; in Appendix C we show standard deviations about the averages for different random initializations. Nevertheless, we have found that the following inequality typically holds, for any given initialization and batch sequences:

$$c_{loss} \leq c_{sharp} \leq c_{max}, \quad (4)$$

except for some outliers due to high fluctuations when the averaged critical curves start merging at large d/w . Figure 5 shows evidence of this for ResNets trained on the CIFAR-10 dataset. Appendix D presents extensive additional results across various architectures.

3.2. Loss connectivity in the early transient period

In the previous subsection, we observed that training loss and sharpness might quickly increase before decreasing (“catapult”) during early training for a range of depths and widths. A logical next step is to analyze the region in the loss landscape that the training reaches after the catapult. A naive intuition would predict a barrier from initialization to the final point after the catapult, as the loss increases during early training. In this section, we will test the credibility of this intuition in real-world models. Specifically, we linearly interpolate the loss between the initial and final point after the catapult and examine the effect of the learning rate, depth, and width. The linearly interpolated loss and barrier are defined as follows.

Definition 3.2. ($\mathcal{L}_{int}(s, c), U(c)$) Let θ_0 represent the initial set of parameters, and let θ_{T_1} represent the set of parameters at the end of the initial transient period, trained using a learning rate constant c . Then, we define the linearly interpolated loss as $\mathcal{L}_{int}(s, c) = \mathcal{L}[(1 - s)\theta_0 + s\theta_{T_1}]$, where $s \in [0, 1]$ is the interpolation parameter. The interpolated loss barrier is defined as the maximum value of the interpolated loss over the range of s : $U(c) = \max_{s \in [0, 1]} \mathcal{L}_{int}(s) - \mathcal{L}(\theta_0)$.

Here we subtracted the loss’s initial value such that a positive value indicates a barrier to the final point from initialization. Using the interpolated loss barrier, we define $c_{barrier}$ as follows.

Definition 3.3. ($c_{barrier}$) Given the initial (θ_0) and final parameters (θ_{T_1}), we define $c_{barrier}$ as the minimum learning rate constant such that there exists a barrier from θ_0 to θ_{T_1}

$$c_{barrier} = \min_c \{c \mid U(c) > 0\} \quad (5)$$

Here, $c_{barrier}$ is also a random variable that depends on the initialization and SGD batch sequence. We denote the average over this randomness using $\langle \cdot \rangle$ as before. Figure 3(c, f) shows the interpolated loss of CNNs trained on the CIFAR-10 dataset for $t = 10$ steps. The experimental setup is the same as in Section 3. For the network with smaller d/w , we observe a barrier emerging at $c_{barrier} = 5.65$, while the loss starts to catapult at $c_{loss} = 2.83$. In comparison, we do not observe any barrier from initialization to the final point at large d/w . Figure 4 shows the relationship between $\langle c_{barrier} \rangle$ and d/w for various models and datasets. We consistently observe that $c_{sharp} \leq c_{barrier}$, suggesting that training traverses a barrier only when sharpness starts to catapult during early training. We chose not to characterize

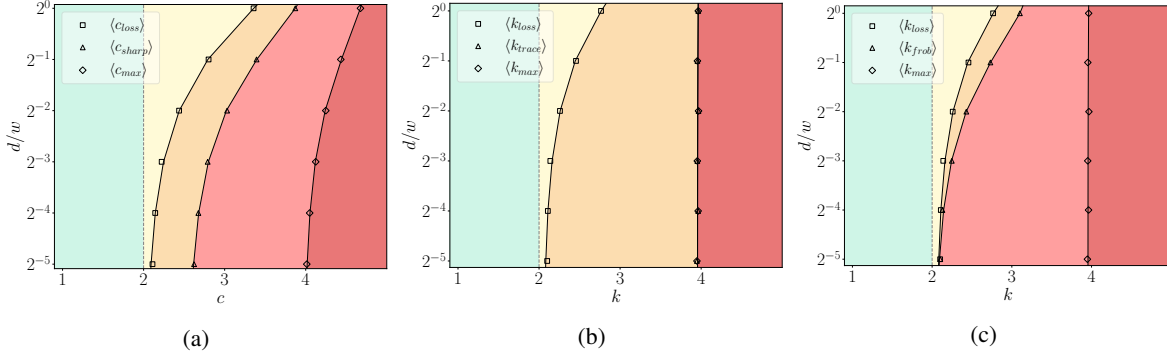


Figure 7. The phase diagram of the uv model trained with MSE loss using gradient descent with (a) the top eigenvalue of Hessian λ_t^H , (b) the trace of Hessian $\text{Tr}(H_t)$ and (c) the square of the Frobenius norm $\text{Tr}(H_t^T H_t)$ used as a measure of sharpness. In (a), the learning rate is scaled as $\eta = c/\lambda_0^H$, while in (b) and (c), the learning rate is scaled as $\eta = k/\text{Tr}(H_0)$. The vertical dashed line shows $c = 2$ for reference. Each data point is an average over 500 random initializations.

the phase diagram of early training using c_{barrier} as we did for other critical c 's, as it is somewhat different in character than the other critical constants, which depend only on the sharpness and loss trajectories.

These observations call into question the intuition of catapulting out of a basin for a range of learning rates in between $c_{\text{loss}} < c < c_{\text{barrier}}$. Instead, these results show that for these learning rates, the final point after the catapult already lies in the same basin as initialization, and even *connected through a linear path*, revealing an inductive bias of the training process towards regions of higher loss during the early time transient regime.

4. Intermediate saturation regimes

In the intermediate saturation regime, the learning rate is small compared to the local sharpness ($\eta < 2/\lambda_t$). As a result, sharpness does not change appreciably and reflects the cumulative change that occurred during the initial transient period. This section analyzes sharpness in the intermediate saturation regime by studying how it changes with the learning rate, depth, and width of the model.

We measure the sharpness λ_τ^H at a time τ in the middle of the intermediate saturation regime. We choose τ so that $c\tau \approx 200$.² For further details on sharpness measurement, see Appendix E.1. Figure 6(a) illustrates the relationship between λ_τ^H and the learning rate for 7-layer deep CNNs trained on the CIFAR-10 dataset with varying widths. The results indicate that the dependence of λ_τ^H on learning rate can be grouped into three distinct stages. (1) At small learning rates, λ_τ^H remains relatively constant, with fluctuations increasing as the ratio of d/w increases ($c < 2$ in Fig. 6(a)).

²In practice time-step $\tau = 200/c$ is in the middle of regime (ii) for the models we studied. Normalizing by c allows proper comparison for different learning rates.

(2) A crossover regime where λ_τ^H is dropping significantly ($2 < c < 2^3$ in Fig. 6(a)). (3) A saturation stage where λ_τ^H stays small and constant with learning rate ($c > 2^3$) in Fig. 6(a). In Appendix E, we show that these results are consistent across architectures and datasets for varying values of d and w . Additionally, the results reveal that in stage (1), where $c < 2$ is sub-critical, λ_τ^H decreases with increasing d/w . In other words, for small c and in the intermediate saturation regime, the loss is locally flatter as d/w increases.

We can precisely extract a critical value of c that separates stages (1) and (2), which corresponds to the onset of an abrupt reduction of sharpness λ_τ^H . To do this, we consider the averaged normalized sharpness over initializations and denote it by $\langle \frac{\lambda_\tau^H}{\lambda_0^H} \rangle$. The first two derivatives of the averaged normalized sharpness, $\chi_\tau = -\frac{\partial}{\partial c} \langle \frac{\lambda_\tau^H}{\lambda_0^H} \rangle$ and $\chi'_\tau = -\frac{\partial^2}{\partial c^2} \langle \frac{\lambda_\tau^H}{\lambda_0^H} \rangle$, characterize the change in sharpness with learning rate. The extrema of χ'_τ quantitatively define the boundaries between the three stages described above. In particular, using the maximum of χ'_τ , we define $\langle c_{\text{crit}} \rangle$, which marks the beginning of the sharp decrease in λ_τ^H with the learning rate.

Definition 4.1. ($\langle c_{\text{crit}} \rangle$) Given the averaged normalized sharpness $\langle \frac{\lambda_\tau^H}{\lambda_0^H} \rangle$ estimated using sharpness measured at τ , we define c_{crit} to be the learning rate constant that minimizes the second derivative of $\langle \frac{\lambda_\tau^H}{\lambda_0^H} \rangle$

$$\langle c_{\text{crit}} \rangle = \arg \min_c \frac{\partial^2}{\partial c^2} \left\langle \frac{\lambda_\tau^H}{\lambda_0^H} \right\rangle = \arg \max_c \chi'_\tau. \quad (6)$$

Here, we use $\langle \cdot \rangle$ to denote that the critical constant is obtained from the averaged normalized sharpness. Figures 6(b, c) show χ_τ and χ'_τ obtained from the results in Figure 6(a). We observe similar results across various architectures and datasets, as shown in Appendix E. Our results show

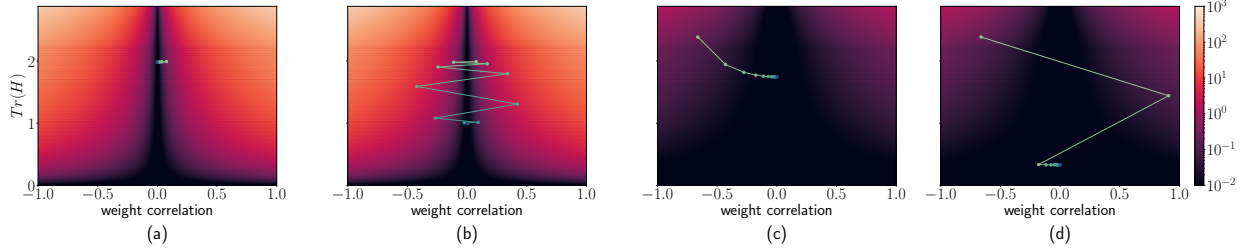


Figure 8. Training trajectories of the uv model, with (a, b) large and (c, d) small width, in a two-dimensional slice of the parameters defined by the trace of Hessian $\text{Tr}(H)$ and weight correlation, trained with (a, c) small ($c = 0.5$) and (b, d) large ($c = 2.5$) learning rates. The colors correspond to the training loss \mathcal{L} , with darker colors representing a smaller loss.

that $\langle c_{crit} \rangle$ has slight fluctuations as d/w is changed, but generally stays in the vicinity of $c = 2$. The peak in χ'_τ becomes wider as d/w increases, indicating that the transition between stages (1) and (2) becomes smoother, presumably due to larger fluctuations in the properties of the Hessian H at initialization. In contrast to $\langle c_{crit} \rangle$, $\langle c_{loss} \rangle$ increases with d/w , implying the opening of the sharpness reduction phase $\langle c_{crit} \rangle < c < \langle c_{loss} \rangle$ as d/w increases.

5. Insights from a simple model

Here we analyze a two-layer linear network (Rennie & Srebro, 2005; Saxe et al., 2014; Lewkowycz et al., 2020), the wv model, which shows much of the phenomena presented above. Define $f(x) = \frac{1}{\sqrt{w}} v^T u x$, with $x, f(x) \in \mathbb{R}$. Here, $u, v \in \mathbb{R}^w$ are the trainable parameters, initialized using the normal distribution, $u_i, v_i \sim \mathcal{N}(0, 1)$ for $i \in \{1, \dots, w\}$. The model is trained with MSE loss on a single training example $(x, y) = (1, 0)$, which simplifies the loss to $\mathcal{L}(u, v) = \frac{1}{2} f^2$. We minimize the loss using gradient descent (GD) with learning rate $\eta = c/\lambda_0^H$.

This model exhibits the (i) early time transient and (ii) intermediate saturation regimes, but not regimes (iii) and (iv).³ The early time phase diagram also shows similar features to those described in preceding sections (compare Fig. 7(a) and Fig. 4). Below we develop an understanding of this early time phase diagram in the wv model.

The update equations of the wv model in function space can be written in terms of the trace of the Hessian $\text{Tr}(H)$.

$$\begin{aligned} f_{t+1} &= f_t \left(1 - \eta \text{Tr}(H_t) + \frac{\eta^2 f_t^2}{w} \right) \\ \text{Tr}(H_{t+1}) &= \text{Tr}(H_t) + \frac{\eta f_t^2}{w} (\eta \text{Tr}(H_t) - 4). \end{aligned} \quad (7)$$

In this model, $\text{Tr}(H)$ is equal to the NTK. From the above equations, it is natural to scale the learning rate as

³For other choices where $y \neq 0$, the model exhibits different phenomenology than discussed here.

$\eta = k/\text{Tr}(H_0)$. Note that $c = \eta \lambda_0^H = k \frac{\lambda_0^H}{\text{Tr}(H_0)}$. Also, we denote the critical constants in this scaling as k_{loss} , k_{trace} , k_{max} and k_{crit} , where the definitions follow from Definitions 3.1 and 4.1 on replacing sharpness with trace. Figure 7(b) shows the phase diagram of early training, with $\text{Tr}(H_t)$ replaced with λ_t^H as the measure of sharpness and with the learning rate scaled as $\eta = k/\text{Tr}(H_0)$. Similar to Figure 7(a), we observe a new phase $\langle k_{crit} \rangle < k < \langle k_{loss} \rangle$ opening up at small width. However, we do not observe the loss-sharpness catapult phase as $\text{Tr}(H)$ does not increase during training (see Equation 7). We also observe $\langle k_{max} \rangle = 4$, independent of width.

In Appendix B.2, we show that

$$\left\langle \frac{\mathcal{L}_1}{\mathcal{L}_0} \right\rangle = (1-k)^2 + \frac{k^2(1-k)}{2(w+1)} + \frac{3k^4}{16(w+1)(w+3)} \quad (8)$$

where the average is over initializations. As explained in Appendix B.2, the critical value of k for which $\langle \mathcal{L}_1/\mathcal{L}_0 \rangle > 1$ increases with $1/w$, which explains why $\langle k_{loss} \rangle$ and $\langle c_{loss} \rangle$ increase with $1/w$. Combined with $k_{crit} \lesssim 2$, this implies the opening up of the sharpness reduction phase as w is decreased.

Figure 8 shows the training trajectories of the wv model with large ($w = 512$) and small ($w = 2$) widths in a two-dimensional slice of parameters defined by $\text{Tr}(H)$ and weight correlation $\frac{\langle v, u \rangle}{\|u\| \|v\|}$. The above figure reveals that the first few training steps of the small-width network take the system in a flatter direction (as measured by $\text{Tr}(H)$) as compared to the wider network. This means that the small-width network needs a relatively larger learning rate to get to a point of increased loss. This means that the loss catapult requires a larger learning rate at a smaller width. We thus have the opening up of a new regime $k_{crit} < k < k_{loss}$, in which the loss and sharpness monotonically decrease during early training. We speculate that similar reasoning holds for real-world models for the opening up of the sharpness reduction phase with increasing d/w .

To understand the loss-sharpness catapult phase, we require

some other measure as $\text{Tr}(H)$ does not increase for $0 < k < 4$. $\lambda_t^H = \|H\|_\infty$ corresponds to the $p = \infty$ Schatten norm, which is difficult to analyze. Instead, we analyze the $p = 2$ Schatten norm, which is the Frobenius norm $\|H\|_F = \sqrt{\text{Tr}(H^T H)}$. For the uv model,

$$\|H_t\|_F^2 = \text{Tr}(H_t^T H_t) = \text{Tr}(H_t)^2 + 4 \left(1 + \frac{2}{w}\right) \mathcal{L}_t \quad (9)$$

We define k_{frob} as the minimum learning rate such that $\|H_t\|_F^2$ increases during early training. Figure 7(c) shows the phase diagram of the uv model, with $\|H_t\|_F^2$ as the measure of sharpness, while the learning rate is scaled as $\eta = k / \text{Tr}(H_0)$. We observe the loss-sharpness catapult phase at small widths, which we understand as follows. In Appendix B.3, we show $\Delta\|H_1\|_F^2 \equiv \|H_1\|_F^2 - \|H_0\|_F^2$ averaged over initializations is

$$\langle \Delta\|H_1\|_F^2 \rangle = I(k, w) + 4 \left(1 + \frac{2}{w}\right) \langle \mathcal{L}_1 - \mathcal{L}_0 \rangle, \quad (10)$$

$I(k, w) = \frac{k(k-4)}{w} \left[\frac{3k(k-4)}{4(w+3)} + 2 \right]$. As demonstrated in Appendix B.3, the critical value for which $\langle \Delta\|H_1\|_F^2 \rangle > 0$ increases from k_{loss} as $1/w$ increases. This explains the existence of the loss-sharpness catapult phase, and the opening up of the loss catapult phase at small w in Fig. 7 (c).

For $k > 4$, both the loss and trace increase initially, causing training to diverge irrespective of width. This yields $c_{max} = 4\lambda_0^H / \text{Tr}(H)$. Figure 10(c) in Appendix B.2 shows that the ratio $\lambda_0^H / \text{Tr}(H_0)$ increases with $1/w$, which explains the increase in $\langle c_{max} \rangle$ with $1/w$.

The loss landscape of the uv model shown in Figure 8 reveals interesting insights into the loss landscape connectivity results in Section 3.2 and the presence of $c_{barrier}$. Fig. 8 shows how even when there is a loss catapult, as long as the learning rate is not too large, the final point after the catapult can be reached from initialization by a linear path without increasing the loss and passing through a barrier. However if the learning rate becomes large enough, then the final point after the catapult may correspond to a region of large weight correlation, and there will be a barrier in the loss upon linear interpolation.

6. Discussion

We have studied the effect of learning rate, depth, and width on the training dynamics in DNNs trained using SGD with learning rate scaled as $\eta = c / \lambda_0^H$. For various models and datasets, we demonstrated the existence of four training regimes. We analyzed the early transient and intermediate saturation regimes and presented a rich phase diagram of early training with learning rate, depth, and width. We report two new phases, sharpness reduction and loss-sharpness catapult, which have not been reported previously. We also

find that the critical c 's increase significantly with d/w on average. We further studied loss connectivity in the early transient regime and demonstrated the existence of a regime $c_{loss} < c < c_{barrier}$, in which the final point after the catapult lies in the same basin as initialization, connected through a linear path. Finally, we study these phenomena in a 2-layer linear network (uv model), gaining insights into the opening of the sharpness reduction phase and increase of c_{max} with d/w .

We performed a preliminary analysis on the effect of batch size on the presented results in Appendix F. The sharpness trajectories of models trained with a smaller batch size ($B = 32$ vs. $B = 512$) show all four training regimes. The main effect of lowering batch size is that in the late time regime (iv), sharpness settles down to a value significantly smaller than $2/\eta$, which is consistent with (Jastrzebski et al., 2020) and (Cohen et al., 2021). In the early transient regime, we observe a qualitatively similar phase diagram. In the intermediate saturation regime, the effect of reducing the batch size is to broaden the transition around c_{crit} .

Throughout this work, we have scaled the learning rate using the top eigenvalue of the Hessian as a measure of sharpness. In practice, various other choices can be made. For example, (Lewkowycz et al., 2020) scaled the learning rate with the top eigenvalue of the NTK, which also shows similar results but a few differences. At early training times, we observed that the NTK may not catapult during early training, which results in the absence of the sharpness catapult phase. Moreover, the deviation of various critical constants, $\langle c_{loss} \rangle$ and $\langle c_{max} \rangle$, with d/w , is less pronounced. These differences can be observed in the uv model analysis presented in Section 5, as $\text{Tr}(H) = \text{NTK}$ in that case.

The early training dynamics is sensitive to the initialization scheme and optimization algorithm used, and we leave it to future work to explore this dependence and its implications. In this work, we focused on models initialized at criticality (Poole et al., 2016) as it allows for proper gradient flow at initialization (Hanin, 2018; Roberts et al., 2022), and studied vanilla SGD for simplicity. However, other initializations (LeCun et al., 2012), parameterizations (Yang & Hu, 2021; Yang et al., 2022), and optimization procedures (Goyal et al., 2017) may show dissimilarities with the reported phase diagram of early training.

Acknowledgements

We thank Andrey Gromov, Tianyu He, and Shubham Jain for discussions, and Paolo Glorioso, Sho Yaida, Daniel Roberts, and Darshil Doshi for detailed comments on the manuscript. This work is supported by an NSF CAREER grant (DMR-1753240) and the Laboratory for Physical Sciences through the Condensed Matter Theory Center.

References

- Achille, A., Rovere, M., and Soatto, S. Critical learning periods in deep neural networks. *ArXiv*, abs/1711.08856, 2017.
- Agarwala, A., Pedregosa, F., and Pennington, J. Second-order regression models exhibit progressive sharpening to the edge of stability. *ArXiv*, abs/2210.04860, 2022.
- Arora, S., Li, Z., and Panigrahi, A. Understanding gradient descent on edge of stability in deep learning. In *International Conference on Machine Learning*, 2022.
- Bradbury, J., Frostig, R., Hawkins, P., Johnson, M. J., Leary, C., Maclaurin, D., Necula, G., Paszke, A., VanderPlas, J., Wanderman-Milne, S., and Zhang, Q. JAX: composable transformations of Python+NumPy programs, 2018. URL <http://github.com/google/jax>.
- Cohen, J. M., Kaur, S., Li, Y., Kolter, J. Z., and Talwalkar, A. S. Gradient descent on neural networks typically occurs at the edge of stability. *ArXiv*, abs/2103.00065, 2021.
- Damian, A., Nichani, E., and Lee, J. D. Self-stabilization: The implicit bias of gradient descent at the edge of stability. *ArXiv*, abs/2209.15594, 2022.
- Dyer, E. and Gur-Ari, G. Asymptotics of wide networks from feynman diagrams. In *International Conference on Learning Representations*, 2020. URL <https://openreview.net/forum?id=S1gFvANKDS>.
- Dziugaite, G. K. and Roy, D. M. Computing nonvacuous generalization bounds for deep (stochastic) neural networks with many more parameters than training data. *arXiv preprint arXiv:1703.11008*, 2017.
- Erhan, D., Bengio, Y., Courville, A., Manzagol, P.-A., Vincent, P., and Bengio, S. Why does unsupervised pre-training help deep learning? *Journal of Machine Learning Research*, 11(19):625–660, 2010. URL <http://jmlr.org/papers/v11/erhan10a.html>.
- Foret, P., Kleiner, A., Mobahi, H., and Neyshabur, B. Sharpness-aware minimization for efficiently improving generalization. *arXiv preprint arXiv:2010.01412*, 2020.
- Fort, S. and Ganguli, S. Emergent properties of the local geometry of neural loss landscapes. *ArXiv*, abs/1910.05929, 2019.
- Fort, S., Dziugaite, G. K., Paul, M., Kharaghani, S., Roy, D. M., and Ganguli, S. Deep learning versus kernel learning: an empirical study of loss landscape geometry and the time evolution of the neural tangent kernel. *ArXiv*, abs/2010.15110, 2020.
- Frankle, J., Dziugaite, G. K., Roy, D. M., and Carbin, M. Linear mode connectivity and the lottery ticket hypothesis. In *Proceedings of the 37th International Conference on Machine Learning*, ICML’20. JMLR.org, 2020.
- Gilmer, J., Ghorbani, B., Garg, A., Kudugunta, S., Neyshabur, B., Cardoze, D. E., Dahl, G. E., Nado, Z., and Firat, O. A loss curvature perspective on training instability in deep learning. *ArXiv*, abs/2110.04369, 2021.
- Goyal, P., Dollár, P., Girshick, R. B., Noordhuis, P., Wesolowski, L., Kyrola, A., Tulloch, A., Jia, Y., and He, K. Accurate, large minibatch sgd: Training imagenet in 1 hour. *ArXiv*, abs/1706.02677, 2017.
- Hanin, B. Which neural net architectures give rise to exploding and vanishing gradients? In *Neural Information Processing Systems*, 2018.
- Hanin, B. and Nica, M. Finite depth and width corrections to the neural tangent kernel. *ArXiv*, abs/1909.05989, 2019.
- He, K., Zhang, X., Ren, S., and Sun, J. Deep residual learning for image recognition. *2016 IEEE Conference on Computer Vision and Pattern Recognition (CVPR)*, pp. 770–778, 2016.
- Heek, J., Levskaya, A., Oliver, A., Ritter, M., Rondepierre, B., Steiner, A., and van Zee, M. Flax: A neural network library and ecosystem for JAX, 2020. URL <http://github.com/google/flax>.
- Hochreiter, S. and Schmidhuber, J. Simplifying neural nets by discovering flat minima. *Advances in neural information processing systems*, 7, 1994.
- Hochreiter, S. and Schmidhuber, J. Flat minima. *Neural computation*, 9(1):1–42, 1997.
- Iyer, G., Hanin, B., and Rolnick, D. Maximal initial learning rates in deep relu networks. *ArXiv*, abs/2212.07295, 2022.
- Jacot, A., Gabriel, F., and Hongler, C. Neural tangent kernel: convergence and generalization in neural networks (invited paper). *Proceedings of the 53rd Annual ACM SIGACT Symposium on Theory of Computing*, 2018.
- Jastrzebski, S., Kenton, Z., Ballas, N., Fischer, A., Bengio, Y., and Storkey, A. J. On the relation between the sharpest directions of dnn loss and the sgd step length. *arXiv: Machine Learning*, 2018.
- Jastrzebski, S., Szymczak, M., Fort, S., Arpit, D., Tabor, J., Cho, K., and Geras, K. J. The break-even point on optimization trajectories of deep neural networks. *ArXiv*, abs/2002.09572, 2020.

- Jiang, Y., Neyshabur, B., Mobahi, H., Krishnan, D., and Bengio, S. Fantastic generalization measures and where to find them. *arXiv preprint arXiv:1912.02178*, 2019.
- Kaplan, J., McCandlish, S., Henighan, T., Brown, T. B., Chess, B., Child, R., Gray, S., Radford, A., Wu, J., and Amodei, D. Scaling laws for neural language models. *arXiv preprint arXiv:2001.08361*, 2020.
- Keskar, N. S., Mudigere, D., Nocedal, J., Smelyanskiy, M., and Tang, P. T. P. On large-batch training for deep learning: Generalization gap and sharp minima. *ArXiv*, abs/1609.04836, 2016.
- Leclerc, G. and Madry, A. The two regimes of deep network training. *ArXiv*, abs/2002.10376, 2020.
- LeCun, Y., Bottou, L., Orr, G. B., and Müller, K.-R. Efficient backprop. In *Neural Networks*, 2012.
- Lee, J., Sohl-dickstein, J., Pennington, J., Novak, R., Schoenholz, S., and Bahri, Y. Deep neural networks as gaussian processes. In *International Conference on Learning Representations*, 2018. URL <https://openreview.net/forum?id=B1EA-M-0Z>.
- Lee, J., Xiao, L., Schoenholz, S. S., Bahri, Y., Novak, R., Sohl-Dickstein, J. N., and Pennington, J. S. Wide neural networks of any depth evolve as linear models under gradient descent. *Journal of Statistical Mechanics: Theory and Experiment*, 2020, 2019.
- Lewkowycz, A., Bahri, Y., Dyer, E., Sohl-Dickstein, J., and Gur-Ari, G. The large learning rate phase of deep learning: the catapult mechanism. *ArXiv*, abs/2003.02218, 2020.
- Meltzer, D. and Liu, J. Catapult dynamics and phase transitions in quadratic nets. *ArXiv*, abs/2301.07737, 2023.
- Poole, B., Lahiri, S., Raghu, M., Sohl-Dickstein, J., and Ganguli, S. Exponential expressivity in deep neural networks through transient chaos. In *NIPS*, 2016.
- Rennie, J. D. M. and Srebro, N. Fast maximum margin matrix factorization for collaborative prediction. In *Proceedings of the 22nd International Conference on Machine Learning*, ICML '05, pp. 713–719, New York, NY, USA, 2005. Association for Computing Machinery. ISBN 1595931805. doi: 10.1145/1102351.1102441. URL <https://doi.org/10.1145/1102351.1102441>.
- Roberts, D. A., Yaida, S., and Hanin, B. *The Principles of Deep Learning Theory*. Cambridge University Press, 2022. <https://deeplearningtheory.com>.
- Savitzky, A. and Golay, M. J. E. Smoothing and differentiation of data by simplified least squares procedures. *Analytical Chemistry*, 36(8):1627–1639, 1964. doi: 10.1021/ac60214a047. URL <https://doi.org/10.1021/ac60214a047>.
- Saxe, A. M., McClelland, J. L., and Ganguli, S. Exact solutions to the nonlinear dynamics of learning in deep linear neural networks. *CoRR*, abs/1312.6120, 2014.
- Shankar, V., Fang, A. W., Guo, W., Fridovich-Keil, S., Schmidt, L., Ragan-Kelley, J., and Recht, B. Neural kernels without tangents. In *ICML*, 2020.
- Sohl-Dickstein, J. N., Novak, R., Schoenholz, S. S., and Lee, J. On the infinite width limit of neural networks with a standard parameterization. *ArXiv*, abs/2001.07301, 2020.
- Virtanen, P., Gommers, R., Oliphant, T. E., Haberland, M., Reddy, T., Cournapeau, D., Burovski, E., Peterson, P., Weckesser, W., Bright, J., van der Walt, S. J., Brett, M., Wilson, J., Millman, K. J., Mayorov, N., Nelson, A. R. J., Jones, E., Kern, R., Larson, E., Carey, C. J., Polat, İ., Feng, Y., Moore, E. W., VanderPlas, J., Laxalde, D., Perktold, J., Cimrman, R., Henriksen, I., Quintero, E. A., Harris, C. R., Archibald, A. M., Ribeiro, A. H., Pedregosa, F., van Mulbregt, P., and SciPy 1.0 Contributors. SciPy 1.0: Fundamental Algorithms for Scientific Computing in Python. *Nature Methods*, 17:261–272, 2020. doi: 10.1038/s41592-019-0686-2.
- Wu, L., Ma, C., and E, W. How sgd selects the global minima in over-parameterized learning: A dynamical stability perspective. In Bengio, S., Wallach, H., Larochelle, H., Grauman, K., Cesa-Bianchi, N., and Garnett, R. (eds.), *Advances in Neural Information Processing Systems*, volume 31. Curran Associates, Inc., 2018. URL <https://proceedings.neurips.cc/paper/2018/file/6651526b6fb8f29a00507de6a49ce30f-Paper.pdf>.
- Yaida, S. Meta-principled family of hyperparameter scaling strategies. *ArXiv*, abs/2210.04909, 2022.
- Yang, G. and Hu, E. J. Tensor programs iv: Feature learning in infinite-width neural networks. In Meila, M. and Zhang, T. (eds.), *Proceedings of the 38th International Conference on Machine Learning*, volume 139 of *Proceedings of Machine Learning Research*, pp. 11727–11737. PMLR, 18–24 Jul 2021. URL <https://proceedings.mlr.press/v139/yang21c.html>.
- Yang, G., Hu, E. J., Babuschkin, I., Sidor, S., Liu, X., Farhi, D., Ryder, N., Pachocki, J. W., Chen, W., and Gao, J. Tensor programs v: Tuning large neural networks via zero-shot hyperparameter transfer. In *Neural Information Processing Systems*, 2022.

Zhu, L., Liu, C., Radhakrishnan, A., and Belkin, M.
Quadratic models for understanding neural network dynamics. *ArXiv*, abs/2205.11787, 2022.

A. Experimental details:

Datasets: We considered the MNIST, Fashion-MNIST, and CIFAR-10 datasets. We standardized the images and used one-hot encoding for the labels.

Models: We considered fully connected networks (FCNs), Myrtle family CNNs (Shankar et al., 2020) and ResNets (version 1) (He et al., 2016) trained using the JAX (Bradbury et al., 2018), and Flax libraries (Heek et al., 2020). We use d and w to denote the depth and width of the network. Below, we provide additional details of the models and clarify what width corresponds to for CNNs and ResNets.

1. **FCNs:** We considered ReLU FCNs with constant width w in Neural Tangent Parameterization (NTP) initialized at criticality (Poole et al., 2016). The models do not include bias or normalization. In this case, the forward pass of the pre-activations from layer l to $l + 1$ is given by

$$h_i^{l+1} = \frac{2}{\sqrt{w}} \sum_j^w W_{ij}^l \phi(h_j^l), \quad (11)$$

where $\phi(\cdot)$ is the ReLU activation and the weights W^l are initialized using a standard normal distribution $W_{ij}^l \sim \mathcal{N}(0, 1)$. We considered $d \in \{4, 8, 16\}$ and $w \in \{256, 512, 1024, 2048\}$.

2. **CNNs:** We considered Myrtle family ReLU CNNs (Shankar et al., 2020) without any bias or normalization in Standard Parameterization (SP), initialized using He initialization (He et al., 2016). The above model uses a fixed number of channels in each layer, which we refer to as the width of the network. In this case, the forward pass equations for the pre-activations from layer l to layer $l + 1$ are given by

$$h_i^{l+1}(\alpha) = \sum_j^w \sum_{\beta \in \ker} W_{ij}^{l+1}(\beta) \phi(h_i^l(\alpha + \beta)), \quad (12)$$

where α, β label the spacial location and the weights are initialized as $W_{ij}^l \sim \mathcal{N}(0, 2/w)$. We considered $d \in \{5, 7, 10\}$ and $w \in \{64, 128, 256\}$.

3. **ResNets:** We considered version 1 ResNet (He et al., 2016) implementations from [Flax examples](#) without Batch Norm or regularization. For ResNets, width corresponds to the number of channels in the first block. For example, the standard ResNet-18 has four blocks with widths $[w, 2w, 4w, 8w]$, with $w = 64$. We refer to w as the width or the widening factor. We considered ResNet-18 and ResNet-34 with $w \in \{32, 64, 128\}$.

All the models are trained with the average loss over the batch $\mathcal{D}_B = (\{x_\mu, y_\mu\}_{\mu=1}^B)$, i.e., $\mathcal{L}(\{x, y\}_{\mathcal{D}_B}) = \frac{1}{B} \sum_{\mu=1}^B \ell(x_\mu, y_\mu)$, where $\ell(\cdot)$ is the loss function. This normalization along with initialization ensures that the loss function is $\mathcal{O}(1)$ at initialization.

We use a batch size of 512 and scale the learning rate as $\eta = c/\lambda_0^H$ in all our experiments, unless specified. The range of c used in experiments is specified in the individual Appendices, [C](#), [E](#), [B](#) and [G](#).

Sharpness measurement: We measure sharpness using the power iteration method with 20 iterations using $m = 2048$ randomly selected training examples. We find that the above setup approximates the sharpness well for various models trained with MSE loss considered in this work.

Averages over initialization and SGD runs: All the critical constants depend on both the random initializations and the SGD runs. In our experiments, we found that the fluctuations from initialization at large d/w outweigh the randomness coming from different SGD runs. Thus, we focus on initialization averages in all our experiments.

A.1. Details of Figures in the main text:

Figure 1: A shallow CNN ($d = 5, w = 128$) trained on the CIFAR-10 dataset with MSE loss for 1000 epochs using SGD with learning rates $\eta = c/\lambda_0^H$ and batch size $B = 512$. To reduce the computational cost, we measure sharpness at every step for the first epoch, every epoch between 10 and 100 epochs, and every 10 epochs beyond 100.

Figure 4: (a) FCNs with $d = 8$ and $w \in \{256, 512, 1024, 2048\}$ trained on the MNIST dataset, (b) CNNs with $d = 7$ and $w \in \{64, 128, 256, 512\}$ trained on the Fashion-MNIST dataset, (c) ResNet with $d = 18$ and $w \in \{32, 64, 128\}$ trained on the CIFAR-10 dataset (without batch normalization). Each data point in the figure represents an average of ten distinct initialization. For additional results, see Appendix C.

Figure 3: (top panel) A wide ($d = 5, w = 512$) and (bottom panel) a deep CNN ($d = 10, w = 128$) trained on the CIFAR-10 dataset with MSE loss for $t = 10$ steps using vanilla SGD with learning rates $\eta = c/\lambda_0^H$ and batch size $B = 512$.

Figure 4: The phase diagrams of the early training of three different types of neural networks trained with MSE loss function using SGD with learning rates $\eta = c/\lambda_0^H$ and batch size $B = 512$. (1) For FCNs, $d \in \{4, 8, 16\}$ and $w \in \{256, 512, 1024, 2048\}$, (2) For CNNs, $d \in \{5, 7, 10\}$ and $w \in \{64, 256, 512, 1024, 2048\}$, (3) For ResNets, $w \in \{32, 64, 128\}$. Additional results are demonstrated in Appendix C. Ten random initializations were considered for each model.

Figure 5: ResNets with $d \in \{18, 34\}$ and $w \in \{32, 64, 128\}$ trained for 10 steps on the CIFAR-10 dataset with MSE loss using vanilla SGD with learning rates $\eta = c/\lambda_0^H$ and batch size $B = 512$. Ten random initializations were considered for each model.

Figure 6: Normalized sharpness measured at $c\tau = 200$ against the learning rate constant for 7-layer CNNs trained on the CIFAR-10 dataset, with $w \in \{128, 256, 512\}$. Each data point is an average over five random initialization. Smoothing details are provided in Appendix E.2.

Figure 7: Phase diagram of the uv model with varying widths $w \in \{2, 4, 8, 16, 32, 64\}$ trained on a single training example $(x, y) = (1, 0)$ with MSE loss using vanilla gradient descent with learning rates scaled as (a) $\eta = c/\lambda_0^H$ and (b) $\eta = k/\text{Tr}(H_0)$, where $c \in [0.1, c_{max}]$, $k \in [0.1, k_{max}]$ in steps of 0.1. (c) The ratio $4/\lambda_0^H/\text{Tr}(H_0)$. Each data point is an average over 500 random initializations.

Figure 8: Training trajectories of the uv model with (a, b) large ($w = 512$) and (c, d) small ($w = 2$) width, trained for $t = 10$ training steps on a single example $(x, y) = (1, 0)$ with MSE loss using vanilla gradient descent with learning rates (a, c) $c = 0.5$ and (b, d) $c = 2.50$.

B. Additional details of the uv model

B.1. The intermediate saturation regime

The uv model does not show the progressive sharpening, and late-time regimes (iii) and (iv) described in the main text. Hence, we can measure sharpness at the end of training to analyze how it is reduced upon increasing the learning rate and to compare with our results for the intermediate saturation regime in more complicated architectures.

Figure 9(a) shows the normalized sharpness measured at $\tau = 100$ steps for various widths. This behavior reproduces the results observed in the intermediate saturation regime in Section 4. In particular, we can see stages (1) and (2), where $\lambda_\tau^H/\lambda_0^H$ starts off fairly independent of learning rate constant c , and then dramatically reduces when $c > 2$; stage (3), where $\lambda_\tau^H/\lambda_0^H$ plateaus at a small value as a function of c is too close to the divergent phase in this model to be clearly observed. The corresponding derivatives of the averaged normalized sharpness, χ_τ , and χ'_τ , are shown in Figure 9(b, c). The vertical dashed lines denote c_{crit} estimated for each width, using the maximum of χ'_τ . We observe that $c_{crit} = 2$ for all widths.

B.2. Opening of the sharpness reduction phase in the uv model

This section shows that $\mathcal{O}(1/w)$ terms in Equation 7 effectively lead to the opening of the sharpness reduction phase with $1/w$ in the uv model. In Appendix B.1, we demonstrated that for the uv model, $c_{crit} = 2$ for all values of widths. Hence, it suffices to show that c_{loss} increases from the value 2 as $1/w$ increases. We do so by finding the smallest k such that the averaged loss (over initializations) increases during early training and then using the relation between λ_0^H and $\text{Tr}(H_0)$ to get an estimate of c_{loss} .

It follows from Equation 7 that the averaged loss at the first step increases if the following holds

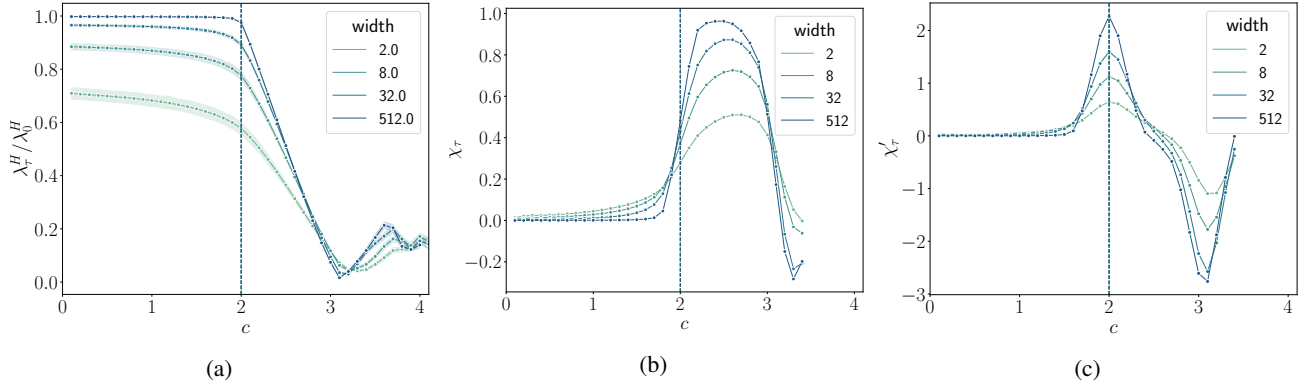


Figure 9. (a) Normalized sharpness measured at $\tau = 100$ steps against the learning rate constant for the uv model trained on $(x, y) = (1, 0)$, with varying widths. Each data point is an average of over 500 initializations, where the shaded region depicts the standard deviation around the mean trend. (b, c) Smooth estimations of the first two derivatives, χ_τ and χ'_τ , of the averaged normalized sharpness wrt the learning rate constant. The vertical dashed lines denote c_{crit} estimated for each width, using the maximum of χ'_τ . Here, we have removed the points beyond $c = 3.5$ for the calculation of derivatives to avoid large fluctuations near the divergent phase. Smoothing details are described in Appendix E.2.

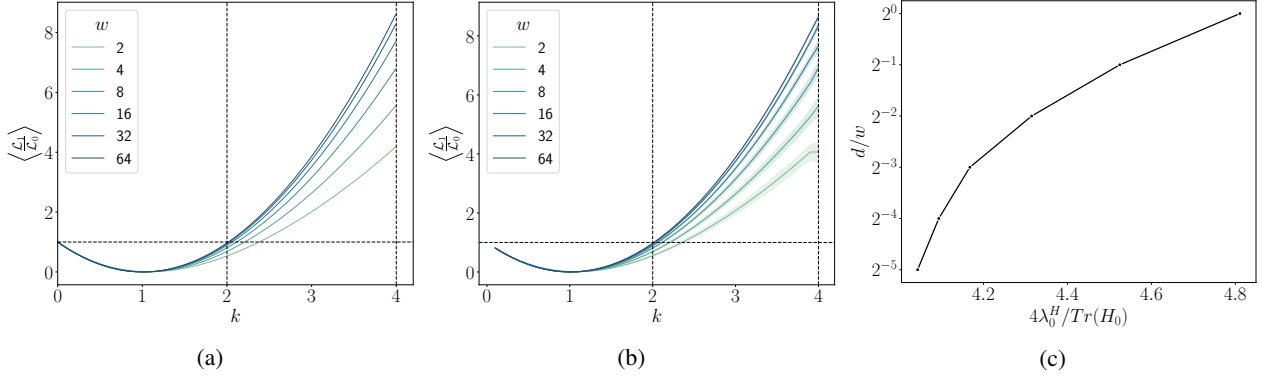


Figure 10. (a, b) The averaged loss at the first step $\langle \frac{\mathcal{L}_1}{\mathcal{L}_0} \rangle$ against the learning rate constant k for varying widths obtained from (a) inequality 17 and (b) numerical experiments. The intersection of $\langle \frac{\mathcal{L}_1}{\mathcal{L}_0} \rangle$ with the horizontal line $y = 1$ depicts k_{loss} . The two vertical lines $k = 2$ and $k = 4$ mark the endpoints of k_{loss} at small and large widths. The shaded region in (b) shows the standard deviation around the mean trend. (c) The scaling of λ_0^H and $\text{Tr}(H_0)$ with width.

$$\left\langle \frac{\mathcal{L}_1}{\mathcal{L}_0} \right\rangle = \left\langle \left(1 - \eta \text{Tr}(H_0) + \frac{\eta^2 f_t^2}{w} \right)^2 \right\rangle > 1, \quad (13)$$

where $\langle \cdot \rangle$ denotes the average over initializations. On scaling the learning rate with trace as $\eta = k/\text{Tr}(H_0)$, we have

$$\left\langle \frac{\mathcal{L}_1}{\mathcal{L}_0} \right\rangle = \left\langle \left(1 - k + \frac{k^2}{w} \frac{f_0^2}{\text{Tr}(H_0)^2} \right) \right\rangle = \left((1 - k)^2 + 2(1 - k) \frac{k^2}{w} \left\langle \frac{f_0^2}{\text{Tr}(H_0)^2} \right\rangle + \frac{k^4}{w^2} \left\langle \frac{f_0^4}{\text{Tr}(H_0)^4} \right\rangle \right) > 1. \quad (14)$$

The required two averages have the following expressions as shown in Appendix B.2.1.

$$\left\langle \frac{f_0^2}{\text{Tr}(H_0)^2} \right\rangle = \frac{w}{4(w+1)} \quad (15)$$

$$\left\langle \frac{f_0^4}{\text{Tr}(H_0)^4} \right\rangle = \frac{3(w+2)w^3}{16} \frac{\Gamma(w)}{\Gamma(w+4)}. \quad (16)$$

Inserting the above expressions in Equation 14, on average the loss increases in the very first step if the following inequality holds

$$\left\langle \frac{\mathcal{L}_1}{\mathcal{L}_0} \right\rangle = \left((1-k)^2 + \frac{k^2(1-k)}{2(w+1)} + \frac{3k^4}{16(w+3)(w+1)} \right) > 1 \quad (17)$$

The graphical representation of the above inequality shown in Figure 10(a) is in excellent agreement with the experimental results presented in Figure 10(b).

Let us denote k'_{loss} as the minimum learning rate constant such that the average loss increases in the first step. Similarly, let k_{loss} denote the learning rate constant if the loss increases in the first 10 steps. Then, k'_{loss} increases from the value 2 as $1/w$ increases as shown in Figure 10(a). By comparison, the trace reduces at any step if $\eta \text{Tr}(H_t) < 4$. At initialization, this condition becomes $k < 4$. Hence, for $k < k'_{loss}$, both the loss and trace monotonically decrease in the first training step. These arguments can be extended to later training steps, revealing that the loss and trace will continue to decrease for $k < k'_{loss}$.

Next, let η_{loss} denote the learning rate corresponding to c_{loss} . Then, we have $\eta_{loss} = \frac{c_{loss}}{\lambda_0^H} = \frac{k_{loss}}{\text{Tr}(H_0)}$, implying

$$c_{loss} = k_{loss} \frac{\lambda_0^H}{\text{Tr}(H_0)}. \quad (18)$$

Figure 10(c) shows that $\lambda_0^H \geq \text{Tr}(H_0)$ for all widths, implying $c_{loss} \geq k_{loss}$. Hence, c_{loss} increases with $1/w$ as observed in Figure 7(a). In Appendix B.1, we demonstrated that for the uv model, $c_{crit} = 2$ for all values of widths. Incorporating this with c_{loss} increases with $1/w$, we have sharpness reduction phase opening up as $1/w$ increases.

B.2.1. DERIVATION OF THE EXPECTATION VALUES

Here, we provide the detailed derivation of the averages $\left\langle \frac{f_0^2}{\text{Tr}(H_0)^2} \right\rangle$ and $\left\langle \frac{f_0^4}{\text{Tr}(H_0)^4} \right\rangle$. We begin by finding the average

$$\left\langle \frac{f_0^2}{\text{Tr}(H_0)^2} \right\rangle$$

$$\left\langle \frac{f_0^2}{\text{Tr}(H_0)^2} \right\rangle = w \int_{-\infty}^{\infty} \prod_{i=1}^w \left(\frac{dv_i du_i}{2\pi} \right) \exp \left(-\frac{\|u\|^2 + \|v\|^2}{2} \right) \frac{\sum_{j,k=1}^w u_j v_j u_k v_k}{(\|u\|^2 + \|v\|^2)^2}, \quad (19)$$

where $\|\cdot\|$ denotes the norm of the vectors.

The above integral is non-zero only if $j = k$. Hence, it is a sum of w identical integrals. Without any loss of generality, we solve this integral for $j = 1$ and multiply by w to obtain the final result, i.e.,

$$\left\langle \frac{f_0^2}{\text{Tr}(H_0)^2} \right\rangle = w^2 \int_{-\infty}^{\infty} \prod_{i=1}^w \left(\frac{dv_i du_i}{2\pi} \right) \exp \left(-\frac{\|u\|^2 + \|v\|^2}{2} \right) \frac{u_1^2 v_1^2}{(\|u\|^2 + \|v\|^2)^2} \quad (20)$$

Consider a transformation of $u, v \in \mathbb{R}^w$ into w dimensional spherical coordinates such that

$$u_1 = r_u \cos \varphi_{u_1}, \quad v_1 = r_v \cos \varphi_{v_1}, \quad (21)$$

which yields,

$$\left\langle \frac{f_0^2}{Tr(H_0)^2} \right\rangle = \frac{w^2}{(2\pi)^w} \int dr_u dr_v d\Omega_{u,w} d\Omega_{v,w} r_u^{w-1} r_v^{w-1} \exp\left(-\frac{r_u^2 + r_v^2}{2}\right) \frac{r_u^2 \cos^2 \varphi_{u_1} r_v^2 \cos^2 \varphi_{v_1}}{(r_u^2 + r_v^2)^2} \quad (22)$$

$$\left\langle \frac{f_0^2}{Tr(H_0)^2} \right\rangle = \frac{w^2}{(2\pi)^w} \int dr_u dr_v \exp\left(-\frac{r_u^2 + r_v^2}{2}\right) \frac{r_u^2 r_v^2}{(r_u^{w+1} + r_v^{w+1})^2} \int d\Omega_{u,w} d\Omega_{v,w} \cos^2 \varphi_{u_1} \cos^2 \varphi_{v_1} \quad (23)$$

$$\left\langle \frac{f_0^2}{Tr(H_0)^2} \right\rangle = \frac{w^2}{(2\pi)^w} \underbrace{\int dr_u dr_v \exp\left(-\frac{r_u^2 + r_v^2}{2}\right) \frac{r_u^2 r_v^2}{(r_u^{w+1} + r_v^{w+1})^2}}_{I_r} \left(\underbrace{\int d\Omega_w \cos^2 \varphi_1}_{I_\varphi} \right)^2, \quad (24)$$

where $d\Omega$ denotes the w dimensional solid angle element. Here, we denote the radial and angular integrals by I_r and I_φ respectively. The radial integral I_r is

$$I_r = \int_0^\infty dr_u dr_v \frac{r_u^{w+1} r_v^{w+1}}{(r_u^2 + r_v^2)^2} \exp\left(-\frac{r_u^2 + r_v^2}{2}\right). \quad (25)$$

Let $r_u = R \cos \theta$ and $r_v = R \sin \theta$ with $R \in [0, \infty)$ and $\theta \in [-\frac{\pi}{2}, \frac{\pi}{2}]$, then we have

$$I_r = \int_0^\infty dR R^{2w-1} e^{-R^2/2} \int_0^{\pi/2} d\theta \cos^{w+1} \theta \sin^{w+1} \theta \quad (26)$$

$$I_r = \frac{\sqrt{\pi} \Gamma(w) \Gamma\left(\frac{w+2}{2}\right)}{2^3 \Gamma\left(\frac{w+3}{2}\right)}, \quad (27)$$

where $\Gamma(\cdot)$ denotes the Gamma function. The angular integral I_φ is

$$I_\varphi = \int d\varphi_1 d\varphi_2 \dots d\varphi_{w-1} \sin^{w-2} \varphi_1 \cos^2 \varphi_1 \sin^{w-3} \varphi_2 \dots \sin \varphi_{w-2} \quad (28)$$

$$I_\varphi = \int d\varphi_1 d\varphi_2 \dots d\varphi_{w-1} \sin^{w-2} \varphi_1 \sin^{w-3} \varphi_2 \dots \sin \varphi_{w-2} \frac{\int_0^\pi d\varphi_1 \sin^{w-2} \varphi_1 \cos^2 \varphi_1}{\int_0^\pi d\varphi_1 \sin^{w-2} \varphi_1} \quad (29)$$

$$I_\varphi = \frac{\pi^{w/2}}{\Gamma\left(\frac{w+2}{2}\right)}. \quad (30)$$

Plugging in Equations 27 and 30 into Equation 24, we obtain a very simple expression

$$\left\langle \frac{f_0^2}{Tr(H_0)^2} \right\rangle = \frac{w^2}{2^{w+3}} \frac{\sqrt{\pi} \Gamma(w)}{\Gamma\left(\frac{w+2}{2}\right) \Gamma\left(\frac{w+3}{2}\right)} = \frac{w}{4(w+1)}. \quad (31)$$

The other integral $\left\langle \frac{f_0^4}{Tr(H_0)^4} \right\rangle$ can be obtained by generalizing the above approach as described below

$$\left\langle \frac{f_0^4}{\text{Tr}(H_0)^4} \right\rangle = w^2 \int_{-\infty}^{\infty} \prod_{i=1}^w \left(\frac{dv_i du_i}{2\pi} \right) \exp \left(-\frac{\|u\|^2 + \|v\|^2}{2} \right) \frac{\sum_{j,k,l,m=1}^w u_j v_j u_k v_k u_l v_l u_m v_m}{(\|u\|^2 + \|v\|^2)^4}. \quad (32)$$

The integral is zero if either $j = k$ and $l = m$ or $j = k = l = m$, which we consider separately. Without loss of generality, we find the following integrals

$$\left\langle \frac{f_0^4}{\text{Tr}(H_0)^4} \right\rangle_{22} = w^2 \int_{-\infty}^{\infty} \prod_{i=1}^w \left(\frac{dv_i du_i}{2\pi} \right) \exp \left(-\frac{\|u\|^2 + \|v\|^2}{2} \right) \frac{u_1^2 u_2^2 v_1^2 v_2^2}{(\|u\|^2 + \|v\|^2)^4} \quad (33)$$

$$\left\langle \frac{f_0^4}{\text{Tr}(H_0)^4} \right\rangle_4 = w^2 \int_{-\infty}^{\infty} \prod_{i=1}^w \left(\frac{dv_i du_i}{2\pi} \right) \exp \left(-\frac{\|u\|^2 + \|v\|^2}{2} \right) \frac{u_1^4 v_1^4}{(\|u\|^2 + \|v\|^2)^4}, \quad (34)$$

which have the following expressions

$$\left\langle \frac{f_0^4}{\text{Tr}(H_0)^4} \right\rangle_{22} = \frac{w^2}{16} \frac{\Gamma(w)}{\Gamma(w+4)} \quad (35)$$

$$\left\langle \frac{f_0^4}{\text{Tr}(H_0)^4} \right\rangle_4 = \frac{9w^2}{16} \frac{\Gamma(w)}{\Gamma(w+4)}, \quad (36)$$

where $\Gamma(\cdot)$ denotes the gamma function. On combining the expressions with their multiplicities, we obtain the final result

$$\left\langle \frac{f_0^4}{\text{Tr}(H_0)^4} \right\rangle = 3w(w-1) \left\langle \frac{f_0^4}{\text{Tr}(H_0)^4} \right\rangle_{22} + w \left\langle \frac{f_0^4}{\text{Tr}(H_0)^4} \right\rangle_4 \quad (37)$$

$$\left\langle \frac{f_0^4}{\text{Tr}(H_0)^4} \right\rangle = \frac{3(w+2)w^3}{16} \frac{\Gamma(w)}{\Gamma(w+4)} \quad (38)$$

B.3. Opening of the loss catapult phase at finite width

In this section, we use the Frobenius norm of the Hessian $\|H\|_F$ as a proxy for the sharpness and demonstrate the emergence of the loss-sharpness catapult phase at finite width. In particular, We analyze the expectation value $\langle \text{Tr}(H^T H) \rangle$ after the first training step near $k = k_{loss}$ and show that $k_{loss} \leq k_{frob}$, with the difference increasing with $1/w$. First, we write $\text{Tr}(H_t^T H_t)$ in terms of \mathcal{L}_t and $\text{Tr}(H_t)$

$$\text{Tr}(H_t^T H_t) = \text{Tr}(H_t)^2 + 4 \left(1 + \frac{2}{w} \right) \mathcal{L}_t. \quad (39)$$

Next, using Equations 7, we write down the change in $\text{Tr}(H_t^T H_t)$ after the first training step in terms of $\text{Tr}(H_0)$ and \mathcal{L}_0

$$\begin{aligned} \Delta \text{Tr}(H_1^T H_1) &= \text{Tr}(H_1^T H_1^T) - \text{Tr}(H_0^T H_0) = \text{Tr}(H_1)^2 - \text{Tr}(H_0)^2 + 4 \left(1 + \frac{2}{w} \right) (\mathcal{L}_1 - \mathcal{L}_0) \\ \Delta \text{Tr}(H_1^T H_1) &= \frac{\eta f_0^2}{w} (\eta \text{Tr}(H_0) - 4) \left[\frac{\eta f_0^2}{w} (\eta \text{Tr}(H_0) - 4) + 2 \text{Tr}(H_0) \right] + 4 \left(1 + \frac{2}{w} \right) (\mathcal{L}_1 - \mathcal{L}_0) \end{aligned} \quad (40)$$

Next, we substitute $\eta = k / \text{Tr}(H_0)$ to obtain the above equation as a function of k

$$\Delta \text{Tr}(H_1^T H_1) = \frac{k(k-4)}{w} \left[\frac{k(k-4)}{w} \frac{f_0^4}{\text{Tr}(H_0)^2} + 2f_0^2 \right] + 4 \left(1 + \frac{2}{w} \right) (\mathcal{L}_1 - \mathcal{L}_0) \quad (41)$$

Finally, we calculate the expectation value of $\langle \Delta \text{Tr}(H_1^T H_1) \rangle$

$$\langle \Delta \text{Tr}(H_1^T H_1) \rangle = \frac{k(k-4)}{w} \left[\frac{k(k-4)}{w} \left\langle \frac{f_0^4}{\text{Tr}(H_0)^2} \right\rangle + 2\langle f_0^2 \rangle \right] + 4 \left(1 + \frac{2}{w} \right) \langle \mathcal{L}_1 - \mathcal{L}_0 \rangle, \quad (42)$$

by estimating $\left\langle \frac{f_0^4}{\text{Tr}(H_0)^2} \right\rangle$ using the approach demonstrated in the previous section

$$\left\langle \frac{f_0^4}{\text{Tr}(H_0)^2} \right\rangle = \frac{3w}{4(w+3)}. \quad (43)$$

Inserting $\left\langle \frac{f_0^4}{\text{Tr}(H_0)^2} \right\rangle$ in Equation 42 along with $\langle f_0^2 \rangle = 1$, we have

$$\langle \Delta \text{Tr}(H_1^T H_1) \rangle = \underbrace{\frac{k(k-4)}{w} \left[\frac{3k(k-4)}{4(w+3)} + 2 \right]}_{I(k,w)} + 4 \left(1 + \frac{2}{w} \right) \langle \mathcal{L}_1 - \mathcal{L}_0 \rangle \quad (44)$$

At infinite width, the above equation reduces to $\langle \Delta \text{Tr}(H_1^T H_1) \rangle = 4 \langle \mathcal{L}_1 - \mathcal{L}_0 \rangle$, and hence, $k_{frob} = k_{loss}$. For any finite width, $I(k, w) < 0$ for $0 < k < 4$. At $k \leq k_{loss}$, $\mathcal{L}_1 - \mathcal{L}_0 \leq 0$, and therefore $\langle \Delta \text{Tr}(H_1^T H_1) \rangle < 0$. In order for the sharpness to catapult, we require $\langle \Delta \text{Tr}(H_1^T H_1) \rangle > 0$ and therefore $k_{frob} > k_{loss}$. As $1/w$ increases $|I(k, w)|$ also increases, which means a higher value of $\mathcal{L}_1 - \mathcal{L}_0$ is required to reach a point where $\langle \Delta \text{Tr}(H_1^T H_1) \rangle \geq 0$. Thus $k_{frob} - k_{loss}$ increases with $1/w$.

B.4. The early training trajectories

Figure 11 shows the early training trajectories of the uv model with large ($w = 512$) and small ($w = 2$) widths. The dynamics depicted show several similarities with early training dynamics of real-world models shown in Figure 3. At small widths, the loss catapults at relatively higher learning rates (specifically, at $c_{loss} = 3.74$, which is significantly higher than the critical value of $c_{crit} = 2$).

B.5. Relationship between critical constants

Figure 12 shows the relationship between various critical constants for the uv model. The data show that the Inequality 4 holds for every random initialization of the uv model.

B.6. Phase diagrams with error bars

This section shows the variation in the phase diagram boundaries of the uv model shown in Figure 7(a, b). Each data point is an average of over 500 initializations and the standard deviation using the error bars.

C. Phase diagrams of early training

This section describes experimental details and shows additional results for the phase diagram of early training. The results include (1) FCNs trained on MNIST, Fashion-MNIST and CIFAR-10 datasets, (2) CNNs trained on Fashion-MNIST and CIFAR-10, (3) ResNets trained on CIFAR-10 datasets. The depths and widths are the same as specified in Appendix A. Figures 14 to 19 show these results.

Phase diagram of training dynamics in DNNs

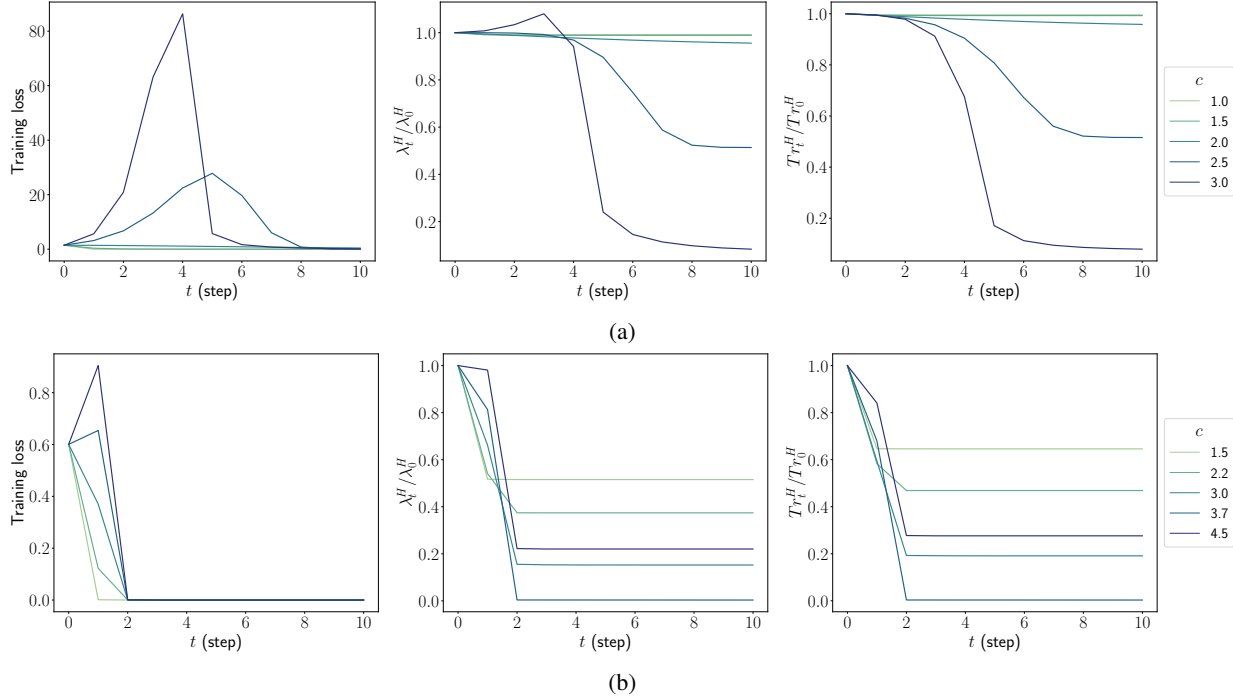


Figure 11. Training trajectories of the uv model with (a, b, c) large ($w = 512$) and (c, d, e) a small ($w = 2$) uv widths trained for $t = 10$ training steps on a single example $(x, y) = (1, 0)$. (a, d) The training loss, (b, e) sharpness, and (c, f) trace of Hessian during early training for the respective models.

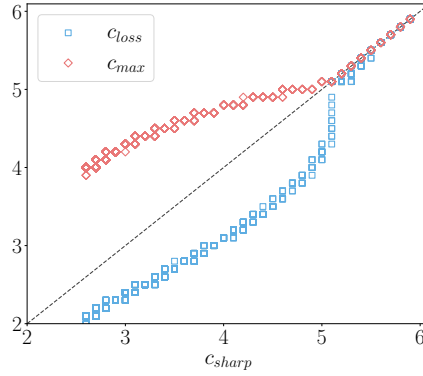


Figure 12. The relationship between the critical constants for the uv model trained on a single training examples $(x, y) = (1, 0)$ with MSE loss using gradient descent. Each data point corresponds to a random initialization

Additional experimental details: We train each model for $t = 10$ steps using SGD with learning rates $\eta = c/\lambda_0^H$ and batch size of 512, where $c = 2^x$ with $x \in \{0.0, \dots, x_{max}\}$ in steps of 0.1. Here, x_{max} is related to the maximum trainable learning rate constant as $c_{max} = 2^{x_{max}}$.

We have considered 10 random initializations for each model. As mentioned in Appendix A, we do not consider averages over SGD runs as the randomness from initialization outweighs it. Hence, we obtain 10 values for each of the critical values in the following results. For each initialization, we compute the critical constants using Definitions 3.1 and 3.3. To avoid a random increase in loss and sharpness due to fluctuations, we round off the values of λ_t^H/λ_0^H and $\mathcal{L}_t/\mathcal{L}_0$ to their second decimal places before comparing with 1. We denote the average values using data points and variation using horizontal bars around the average data points, which indicate the region between 25% and 75% quantile. The smooth curves are obtained by fitting a 2 degree polynomial, except for ResNets, for which we fit a linear line.

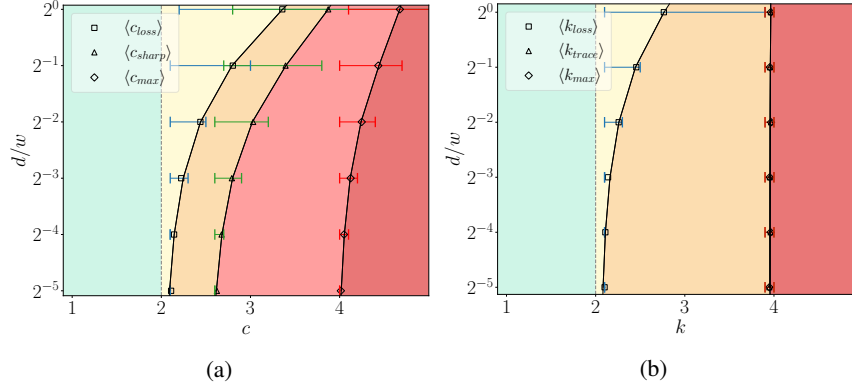


Figure 13. The phase diagram of the uv model trained with MSE loss using gradient descent with learning rates scaled with (a) sharpness $\eta = c/\lambda_0^H$ and (b) trace of Hessian $\eta = k/\text{Tr}_0^H$. Each data point denotes an average of over 500 initialization, and the smooth curve represents a 2 degree polynomial fitted to the raw data. The horizontal bars around the average data point indicate the region between 25% and 75% quantile.

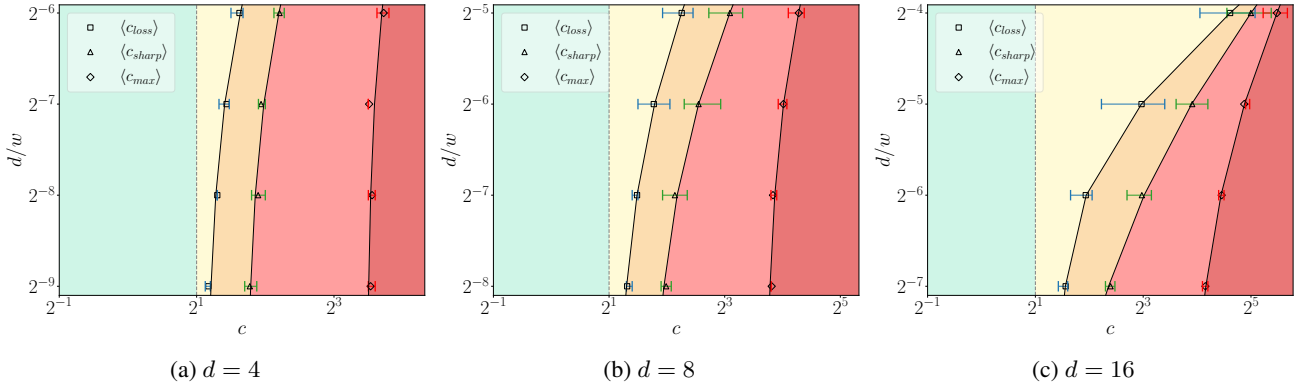


Figure 14. Phase diagrams of fully connected networks (FCNs) with varying depths trained on the MNIST dataset.

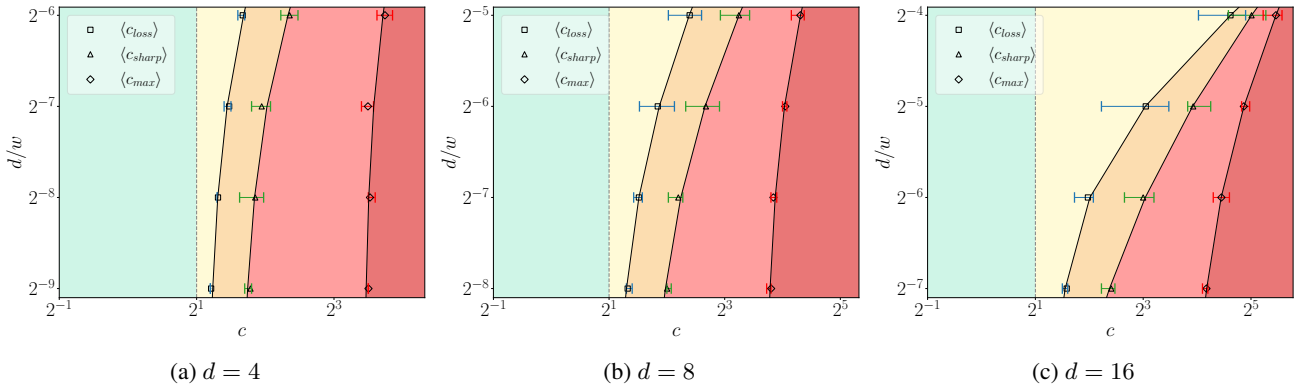


Figure 15. Phase diagrams of fully connected networks (FCNs) with varying depths trained on the Fashion-MNIST dataset.

D. Relationship between various critical constants

Figure 20 illustrates the relationship between the early training critical constants for models and datasets. The experimental setup is the same as in Appendix C. Typically, we find that $c_{loss} \leq c_{sharp} \leq c_{max}$ holds true. However, there are some exceptions, which are observed at high values of d/w (see 20 (d, e)), where the trends of the critical constants converge and large fluctuations can cause deviations from the inequality.

Phase diagram of training dynamics in DNNs

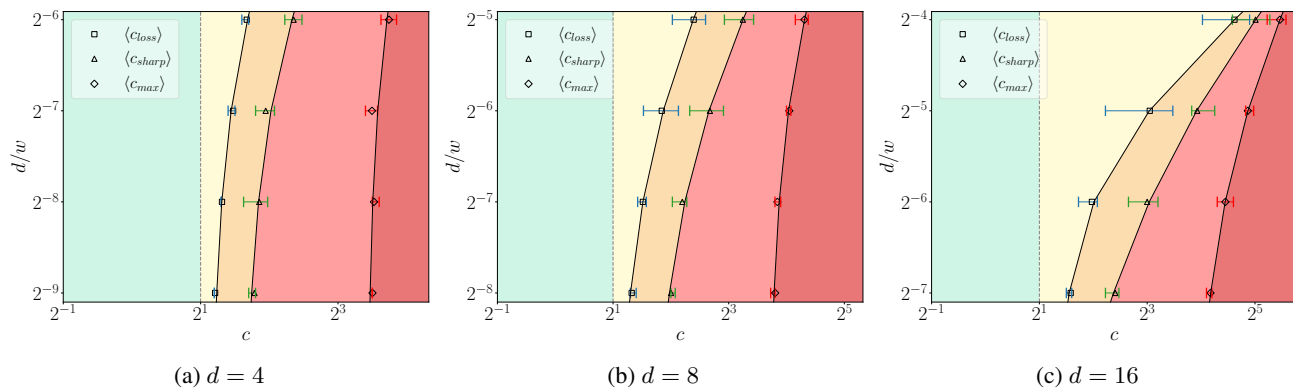


Figure 16. Phase diagrams of fully connected networks (FCNs) with varying depths trained on the CIFAR-10 dataset.

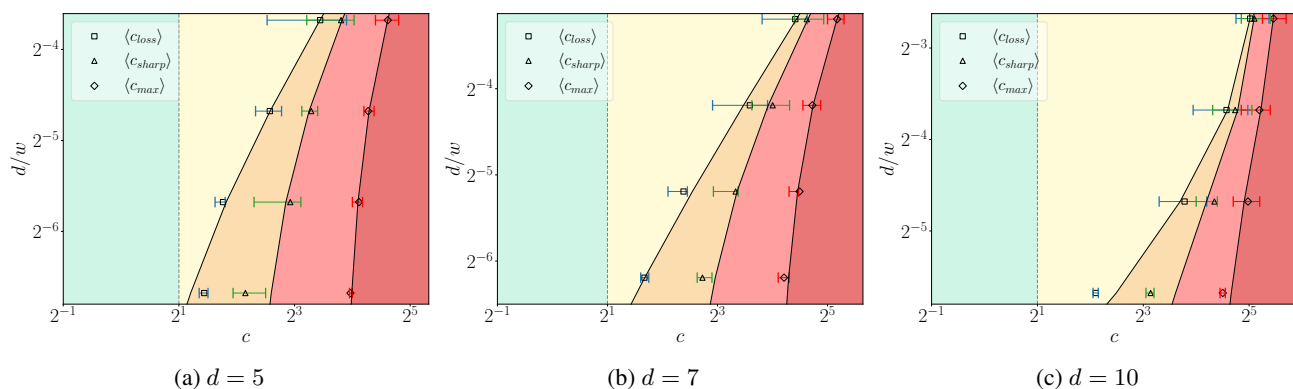


Figure 17. Phase diagrams of Convolutional Neural Networks (CNNs) with varying depths trained on the Fashion-MNIST dataset.

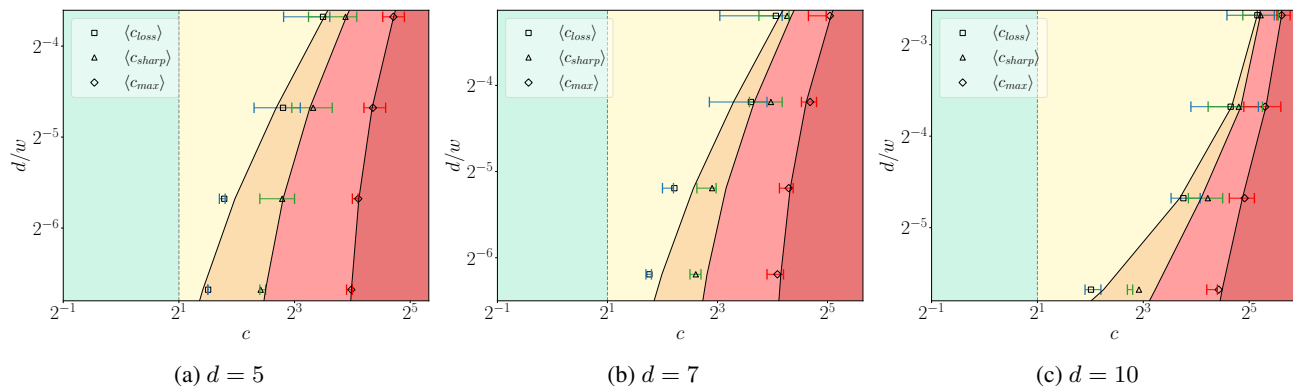


Figure 18. Phase diagrams of Convolutional Neural Networks (CNNs) with varying depths trained on the Fashion-MNIST dataset.

E. Sharpness curves in the intermediate saturation regime

This section shows additional results for Section 4. Figures 21 to 25 show the normalized sharpness curves for different depths and widths.

E.1. Estimating the sharpness

This paragraph describes the procedure for measuring the sharpness to study the effect of the learning rate, depth, and width in the intermediate saturation regime. We measure the sharpness λ_{τ}^H at a time τ in the middle of the intermediate saturation

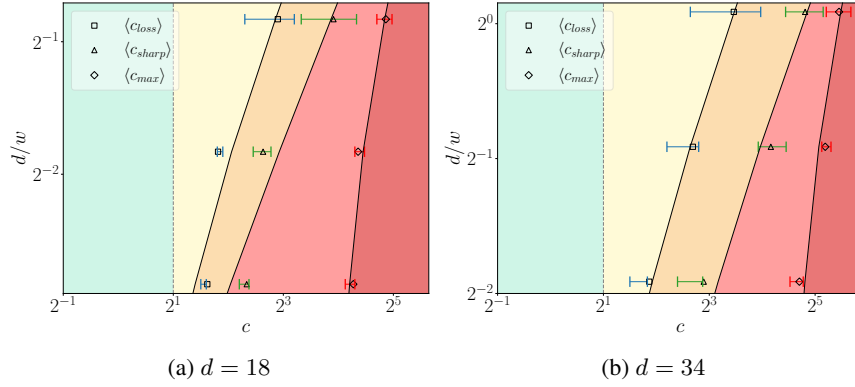
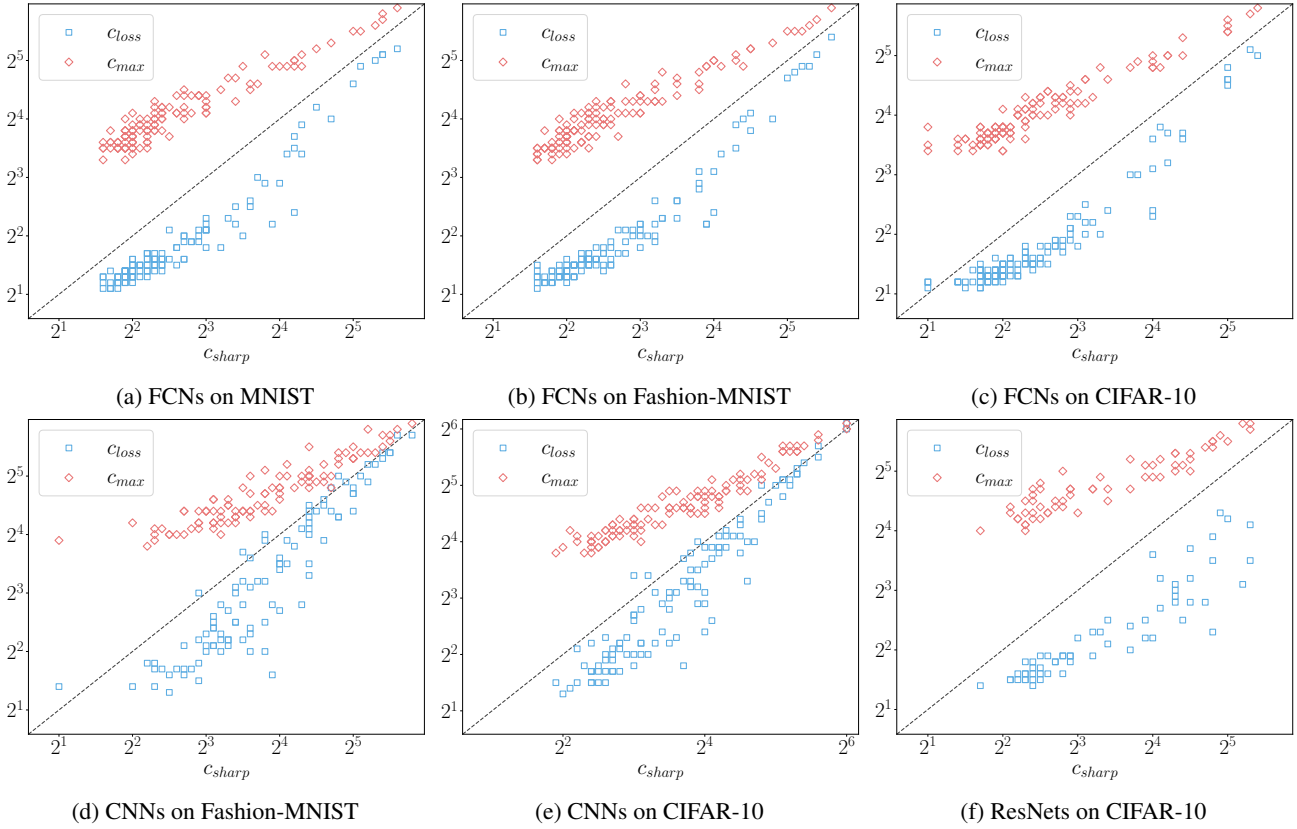


Figure 19. Phase diagrams of Resnets with different depths trained on the CIFAR-10 dataset.


 Figure 20. The relationship between various critical constants for various models and datasets. Each data point corresponds to a model with random initialization. The dashed line denotes the values where $x = y$.

regime. We choose τ so that $c\tau \approx 200$, for learning rates $c = 2^x$, where $x \in [-1.0, 4.0]$ in steps of 0.1. The value 200 is chosen such that τ is in the middle of the intermediate saturation regime. Next, we measure sharpness over a range of steps $t \in [\tau - 5, \tau + 5]$ and average over t to reduce fluctuations. We repeat this process for various initializations and obtain the average sharpness.

E.2. Estimating the critical constant c_{crit}

This subsection explains how to estimate c_{crit} from sharpness measured at time τ . First, we normalize the sharpness with its initial value, and then average over random initializations. Next, we estimate the critical point c_{crit} using the second

Phase diagram of training dynamics in DNNs

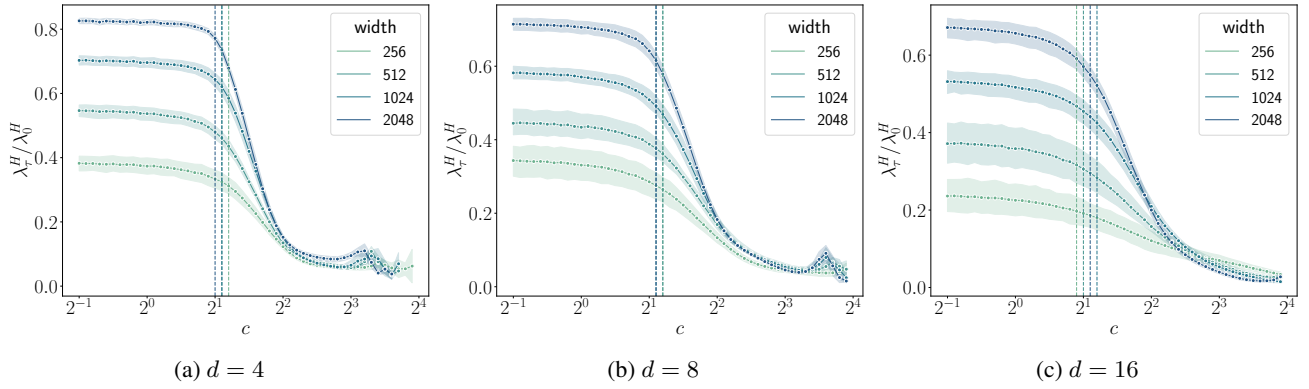


Figure 21. Sharpness measured at $\tau = 200$ against the learning rate constant for FCNs trained on the MNIST dataset, with varying depths and widths. Each curve is an average over ten initializations, where the shaded region depicts the standard deviation around the mean trend. The vertical dashed line shows $c = 2$ for reference.

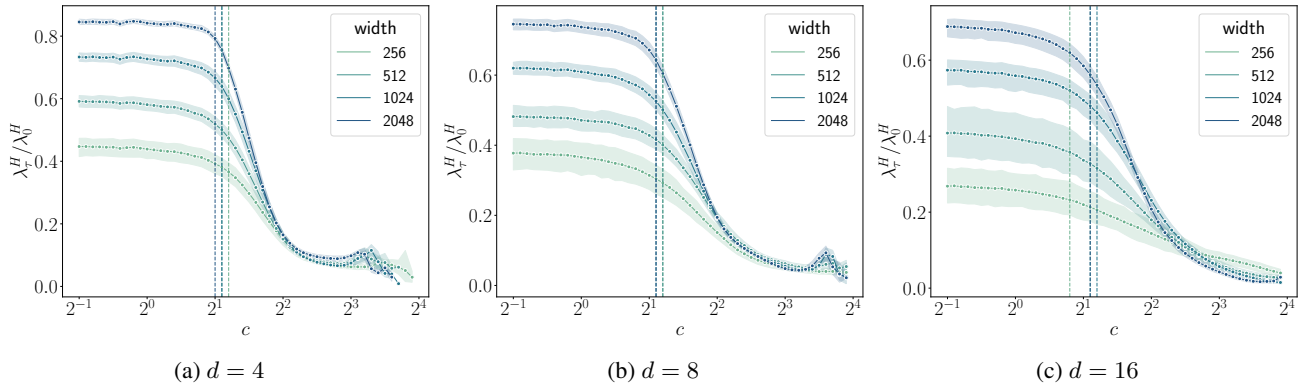


Figure 22. Sharpness measured at $\tau = 200$ against the learning rate constant for FCNs trained on the Fashion-MNIST dataset, with varying depths and widths. Each curve is an average over ten initializations, where the shaded region depicts the standard deviation around the mean trend. The vertical dashed line shows $c = 2$ for reference.

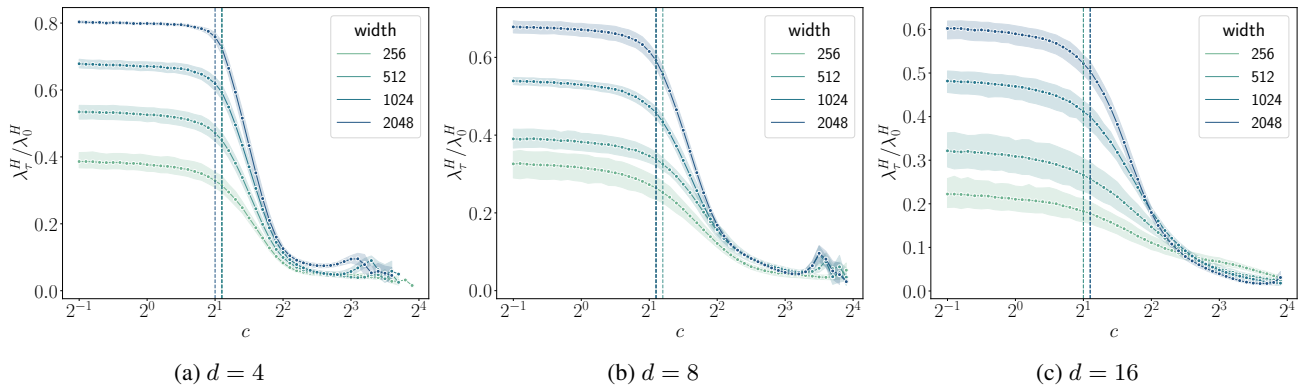


Figure 23. Sharpness measured at $\tau = 200$ against the learning rate constant for FCNs trained on the CIFAR-10 dataset, with varying depths and widths. Each curve is an average over ten initializations, where the shaded region depicts the standard deviation around the mean trend. The vertical dashed line shows $c = 2$ for reference.

derivative of the order parameter curve. Even if the obtained averaged normalized sharpness curve is somewhat smooth, the second derivative may become extremely noisy as minor fluctuations amplify on taking derivatives. This can cause difficulties in obtaining c_{crit} . We resolve this issue by estimating the smooth derivatives of the averaged order parameter with

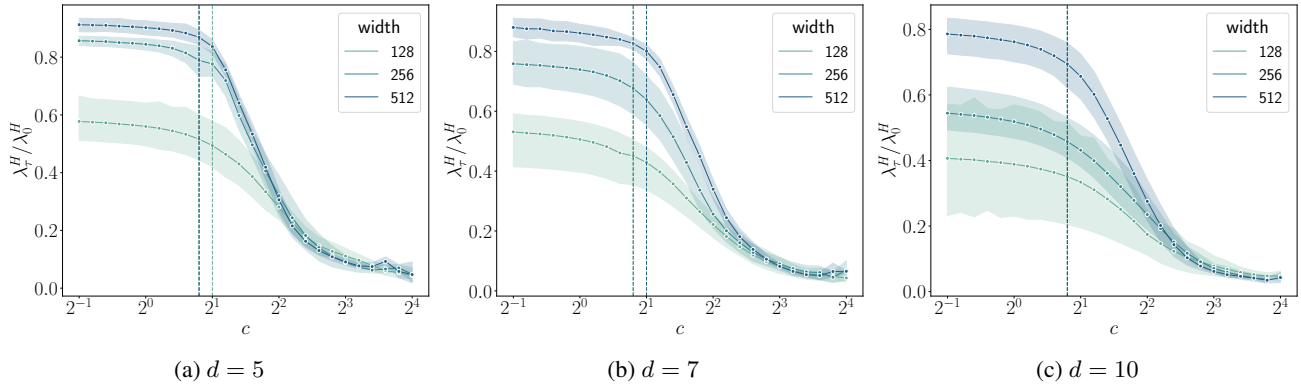


Figure 24. Sharpness measured at $\tau = 200$ against the learning rate constant for Myrtle-CNNs trained on the CIFAR-10 dataset, with varying depths and widths. Each curve is an average of over ten initializations, where the shaded region depicts the standard deviation around the mean trend. The vertical dashed line shows $c = 2$ for reference.

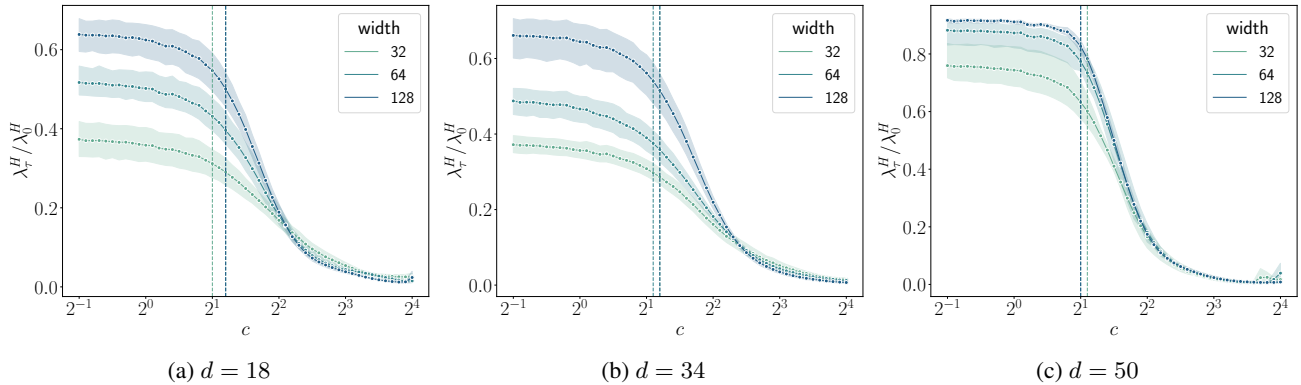


Figure 25. Sharpness measured at $\tau = 200$ against the learning rate constant for ResNets trained on the CIFAR-10 dataset, with varying depths and widths. Each curve is an average of over ten initializations, where the shaded region depicts the standard deviation around the mean trend. The vertical dashed line shows $c = 2$ for reference.

the Savitzky–Golay filter (Savitzky & Golay, 1964) using its scipy implementation (Virtanen et al., 2020). The estimated c_{crit} is shown by vertical lines in the sharpness curves in Figures 21 to 25.

F. The effect of batch size on the reported results

F.1. The four training regimes

Figure 26 shows the sharpness trajectories for CNNs trained with a batch size of 32. We observe that regimes (i) and (ii) show qualitatively the same behavior. In contrast, we observe that the sharpness settles down to a significantly smaller value at late training times, which is consistent with Jastrzebski et al. (Jastrzebski et al., 2020) and Cohen et al. (Cohen et al., 2021).

F.2. The early transient regime

Figure 27 shows the phase diagrams of early training dynamics of FCNs with $d = 4$ trained on the CIFAR-10 dataset using two different batch sizes. The phase diagram obtained is consistent with the findings presented in Section 3, except for one key difference. Specifically, we observe that when d/w is small and small batch sizes are used for training, sharpness may increase from initialization at relatively smaller values of c . This is reflected in Fig. 27 by $\langle c_{sharp} \rangle$ moving to the left as B is reduced from 512 to 128. However, this initial increase in sharpness is small compared to the sharpness catapult observed at larger batch sizes. We found that this increase at small batch sizes is due to fluctuations in gradient estimation that can

Phase diagram of training dynamics in DNNs

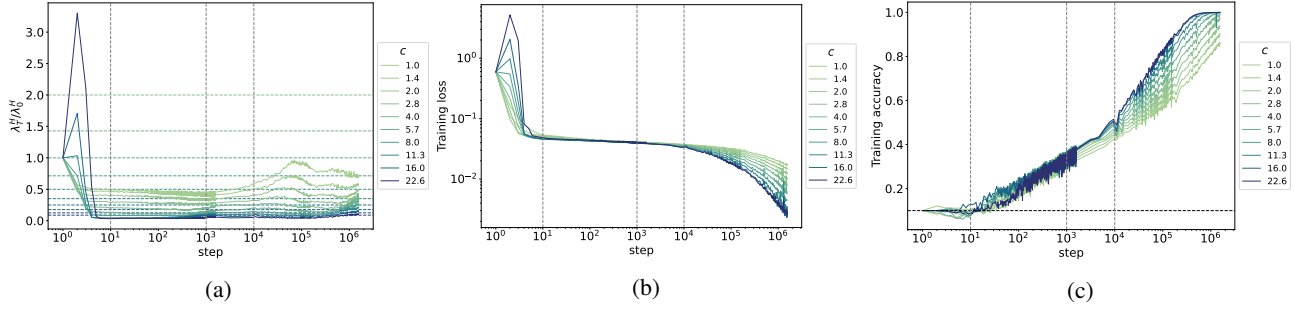


Figure 26. CNN with $d = 5$ and $w = 128$ trained on the CIFAR-10 dataset with MSE loss using vanilla SGD for 1000 epochs with a batch size $B = 32$.

cause sharpness to increase above its initial value by chance.

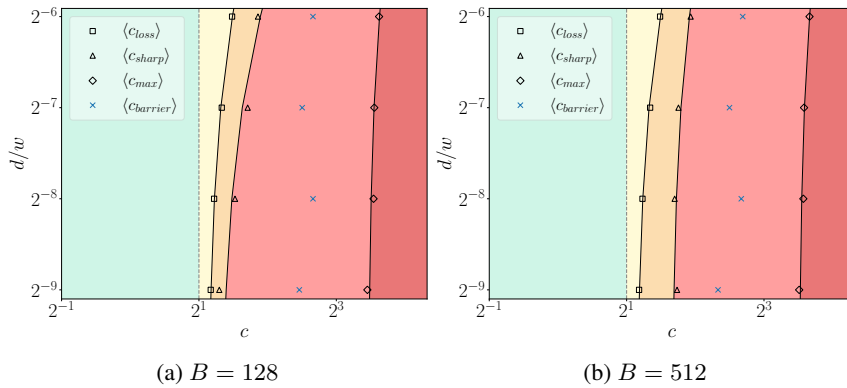


Figure 27. The phase diagram of early training for FCNs with $d = 4$ trained on the CIFAR-10 dataset with MSE loss using SGD with different batch sizes.

F.3. The intermediate saturation regime

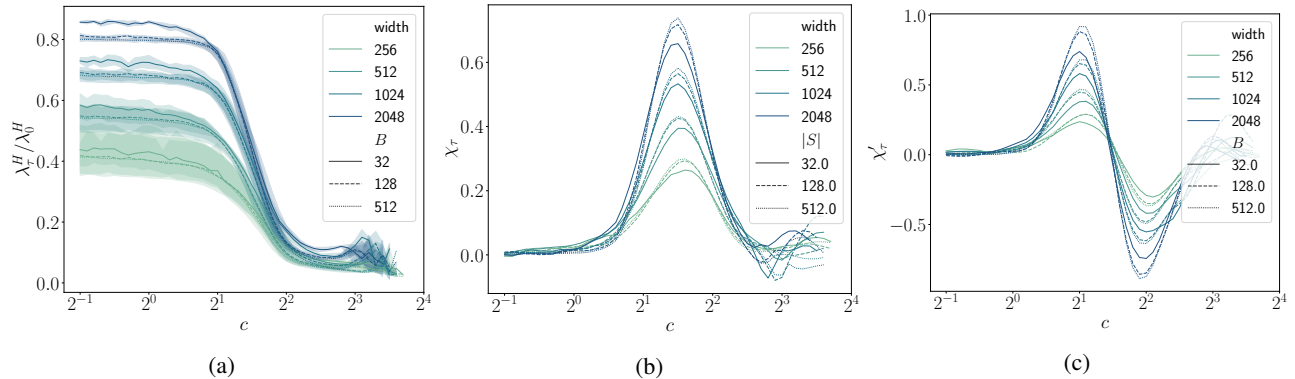


Figure 28. (a) Normalized sharpness measured at $c\tau = 200$ against the learning rate constant for FCNs with $d = 4$ trained on the CIFAR-10 dataset, with varying widths. Each data point is an average over 10 initializations, where the shaded region depicts the standard deviation around the mean trend. (b, c) Smooth estimations of the first two derivatives, χ_τ and χ'_τ , of the averaged normalized sharpness wrt the learning rate constant.

Figure 28 shows the normalized sharpness, measured at $c\tau = 200$, and its derivatives for various widths and batch sizes. The results are consistent with those in Section 4, with a lowering in the peak heights of the derivatives χ and χ' at small batch sizes. The lowering of the peak heights means the full width at half maximum increases, which implies a broadening

of the transition around c_{crit} at smaller batch sizes.

G. The four regimes of training

This section shows that various models trained on different datasets may show the four training regimes. We train FCNs, CNNs, and ResNets on MNIST, Fashion-MNIST, and CIFAR-10 datasets using MSE and CSE loss using SGD. An exception to the observation is that FCNs with large widths did not exhibit the late-time regime, even after training for 1000 epochs, which is consistent with (Cohen et al., 2021). We scale the learning rate as $\eta = c/\lambda_0^H$, where $c = 2^x$ with $x \in \{0.0, 0.5, \dots, x_{max}\}$, where x_{max} corresponds to the maximum trainable learning rate η_{max} . To reduce computational time, we measure sharpness at every step in the first epoch and every epoch thereafter. Figure 29 to 52 show the training trajectories of various architectures and datasets. Additional details of the experiments are provided in the figure captions.

For the cross-entropy loss, the late time regime is significantly more complex than the case of MSE loss. The sharpness oscillates wildly when the edge of stability threshold is reached, and in some cases, sharpness dramatically drops again after this point.

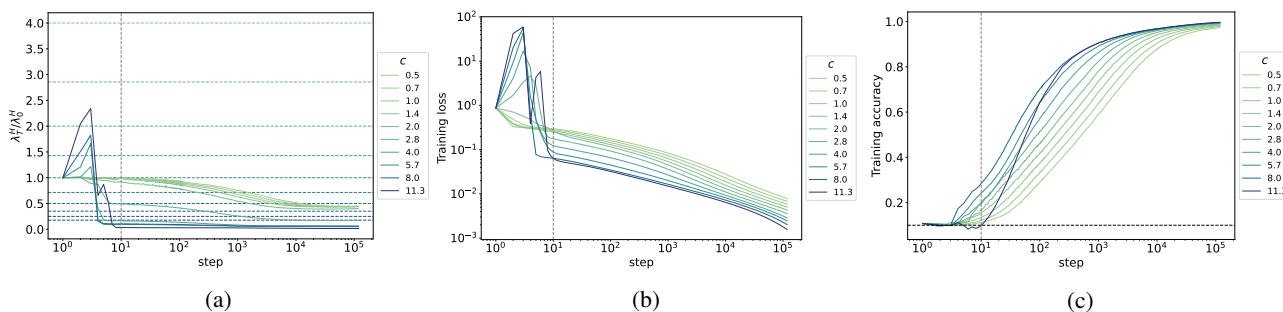


Figure 29. FCN with $d = 4$ and $w = 2048$ trained on the MNIST dataset with MSE loss using vanilla SGD for 1000 epochs with a batch size $B = 512$.

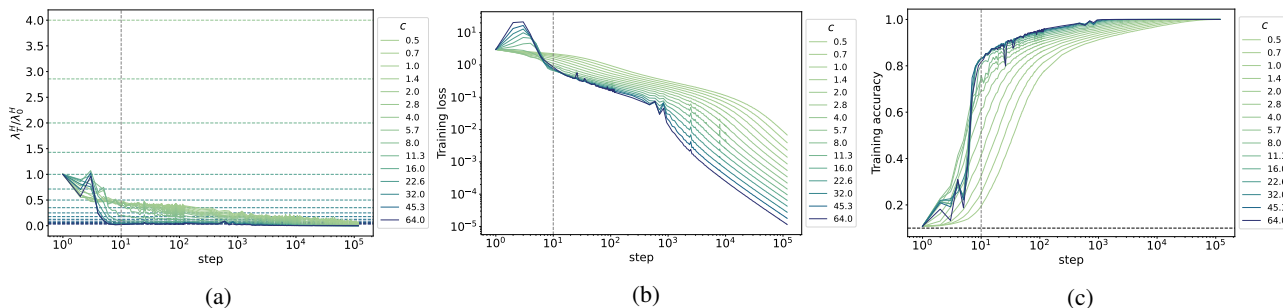


Figure 30. FCN with $d = 4$ and $w = 2048$ trained on the MNIST dataset with cross-entropy loss using vanilla SGD for 1000 epochs with a batch size $B = 512$.

G.1. Training trajectories with training time scaled with learning rate

In this section, we show the training trajectories against the scaled training time $\tilde{t} = c \cdot t$. Figures 53 to 64 show these results.

Phase diagram of training dynamics in DNNs

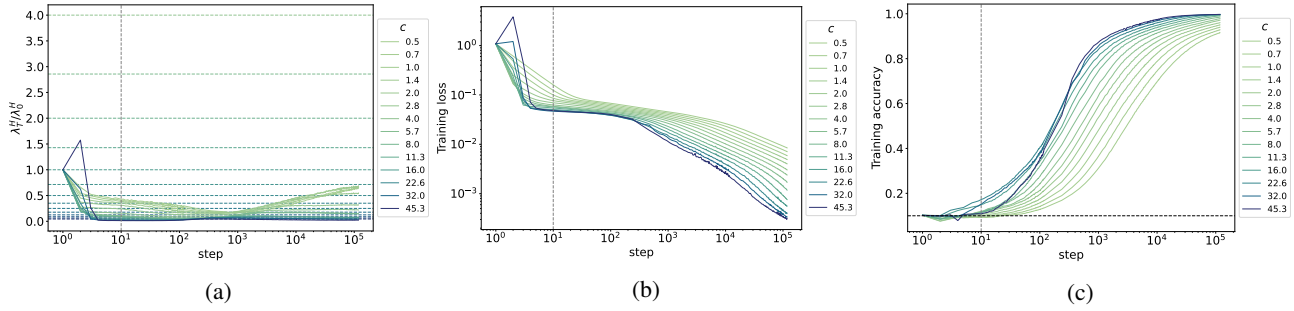


Figure 31. FCN with $d = 16$ and $w = 256$ trained on the MNIST dataset with MSE loss using vanilla SGD for 1000 epochs with a batch size $B = 512$.

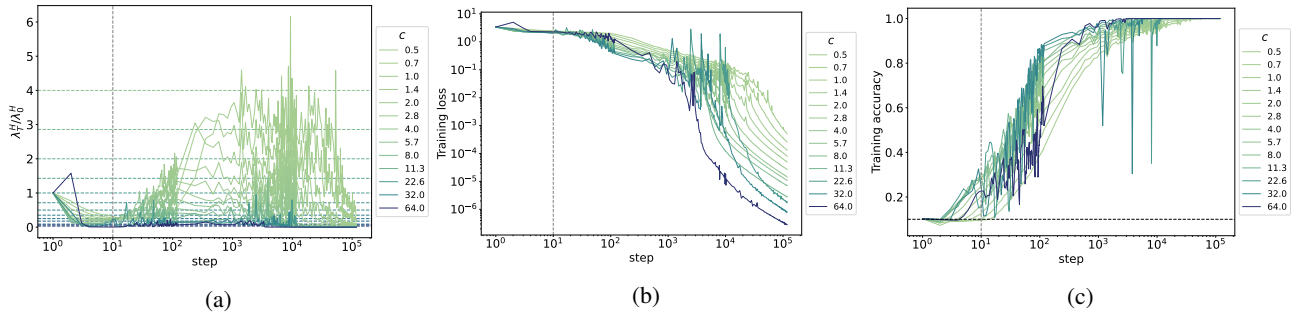


Figure 32. FCN with $d = 16$ and $w = 256$ trained on the MNIST dataset with cross-entropy loss using vanilla SGD for 1000 epochs with a batch size $B = 512$.

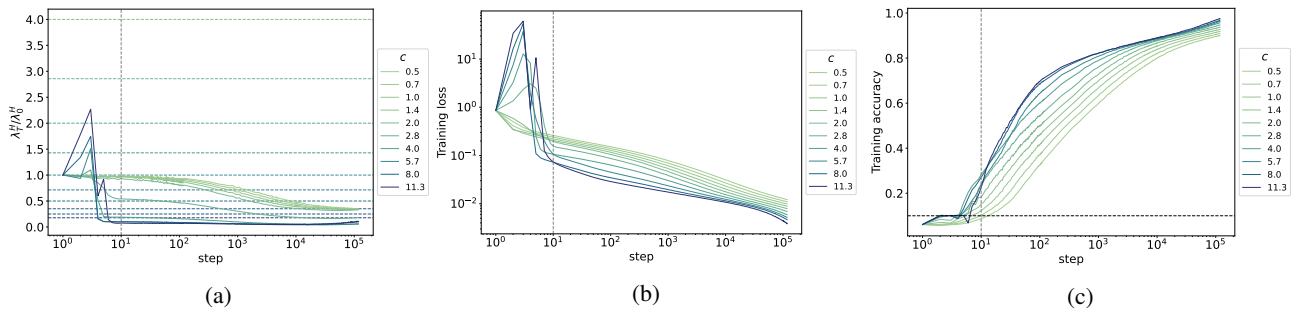


Figure 33. FCN with $d = 4$ and $w = 2048$ trained on the Fashion-MNIST dataset with MSE loss using vanilla SGD for 1000 epochs with a batch size $B = 512$.

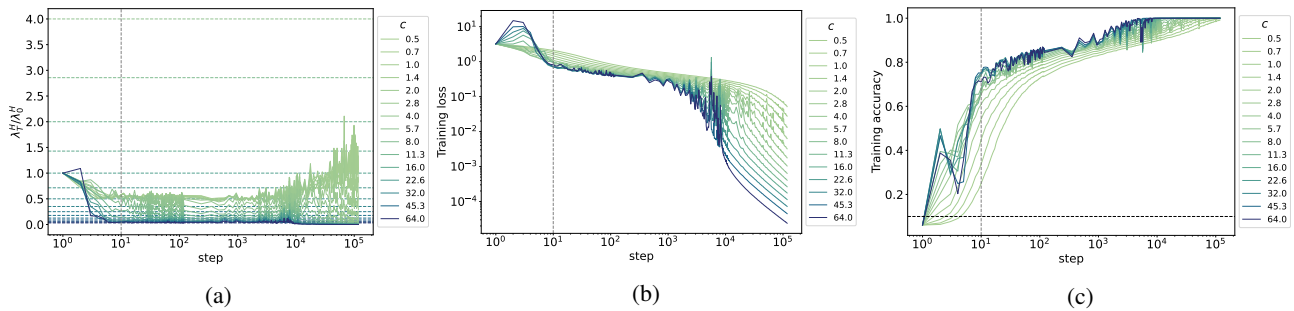


Figure 34. FCN with $d = 4$ and $w = 2048$ trained on the Fashion-MNIST dataset with cross-entropy loss using vanilla SGD for 1000 epochs with a batch size $B = 512$.

Phase diagram of training dynamics in DNNs

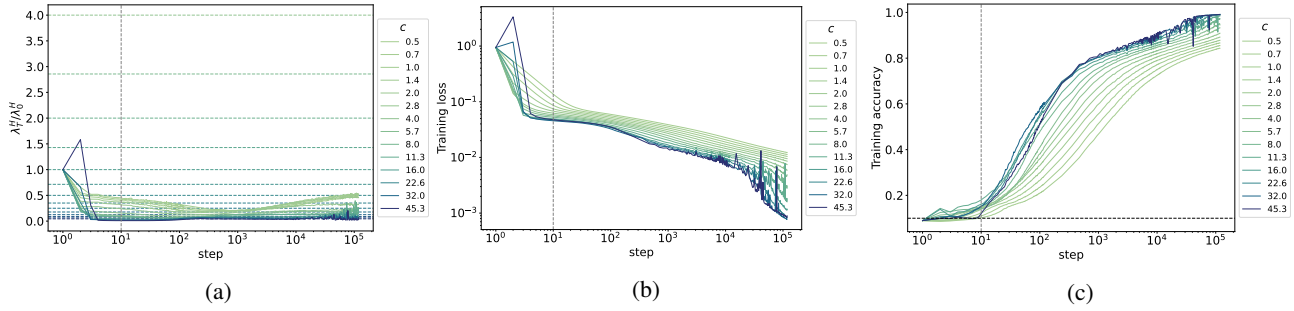


Figure 35. FCN with $d = 16$ and $w = 256$ trained on the Fashion-MNIST dataset with MSE loss using vanilla SGD for 1000 epochs with a batch size $B = 512$.

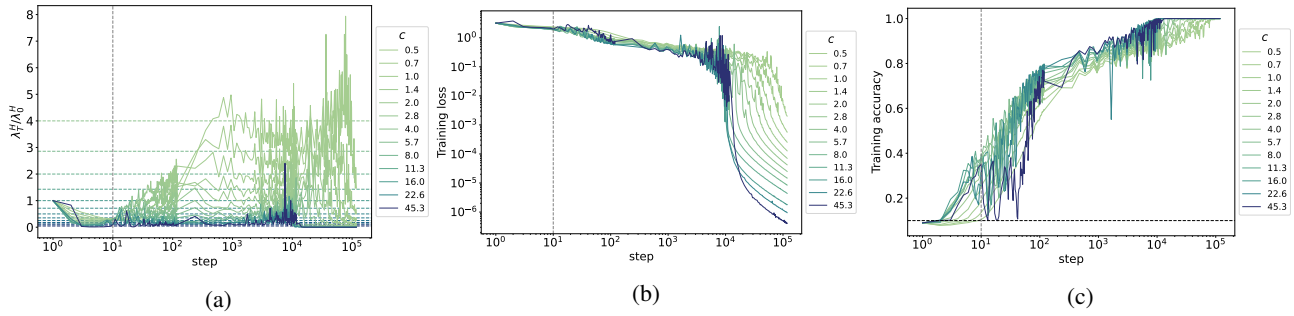


Figure 36. FCN with $d = 16$ and $w = 256$ trained on the Fashion-MNIST dataset with cross-entropy loss using vanilla SGD for 1000 epochs with a batch size $B = 512$.

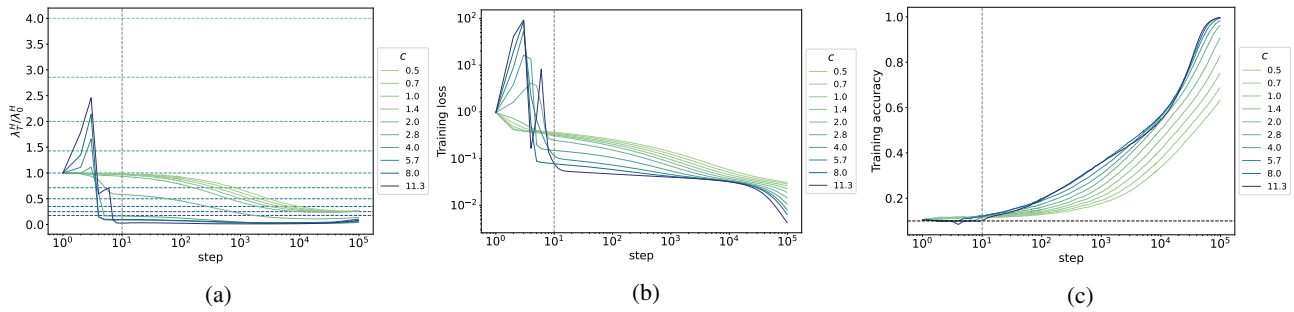


Figure 37. FCN with $d = 4$ and $w = 2048$ trained on the CIFAR-10 dataset with MSE loss using vanilla SGD for 1000 epochs with a batch size $B = 512$.

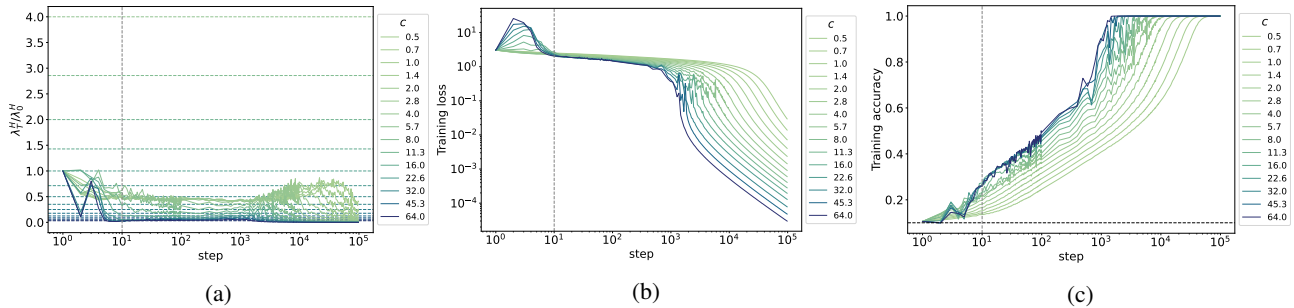


Figure 38. FCN with $d = 4$ and $w = 2048$ trained on the CIFAR-10 dataset with cross-entropy loss using vanilla SGD for 1000 epochs with a batch size $B = 512$.

Phase diagram of training dynamics in DNNs

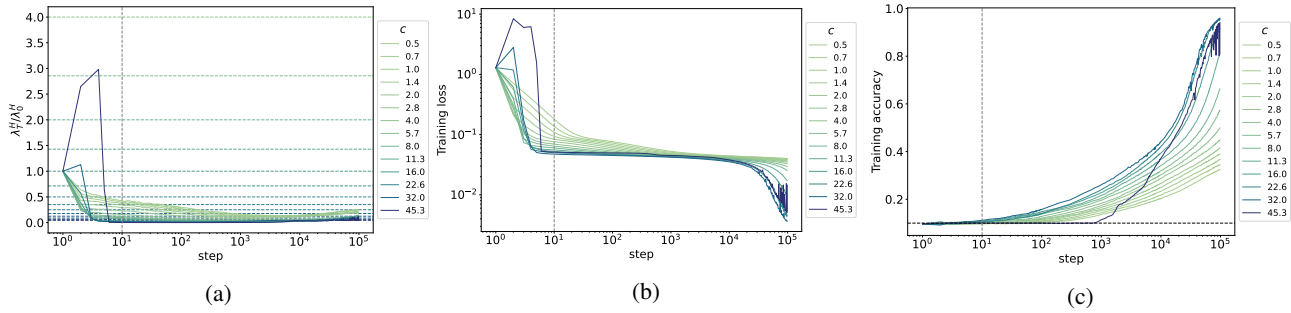


Figure 39. FCN with $d = 16$ and $w = 256$ trained on the CIFAR-10 dataset with MSE loss using vanilla SGD for 1000 epochs with a batch size $B = 512$.

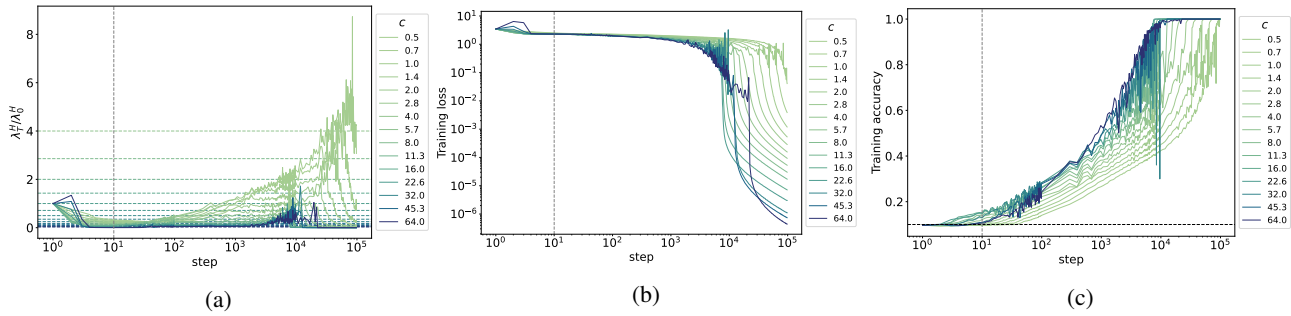


Figure 40. FCN with $d = 16$ and $w = 256$ trained on the CIFAR-10 dataset with cross-entropy loss using vanilla SGD for 1000 epochs with a batch size $B = 512$.

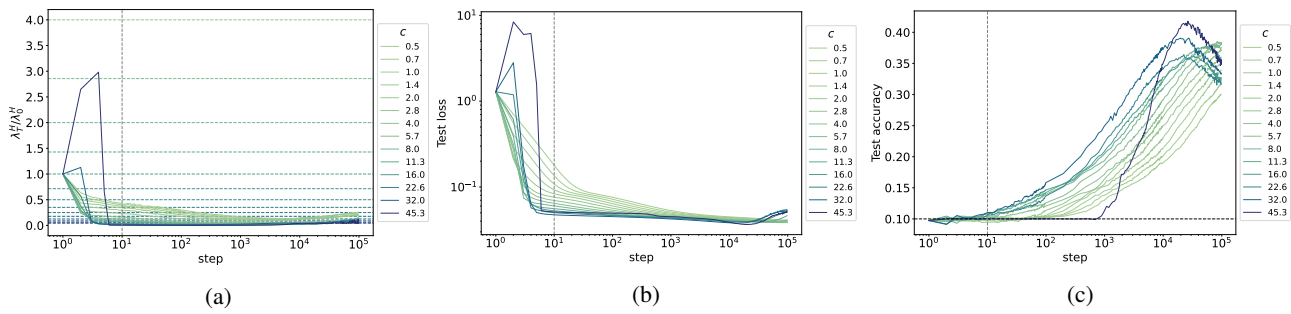


Figure 41. FCN with $d = 16$ and $w = 256$ trained on the CIFAR-10 dataset with MSE loss using vanilla SGD for 1000 epochs with a batch size $B = 512$.

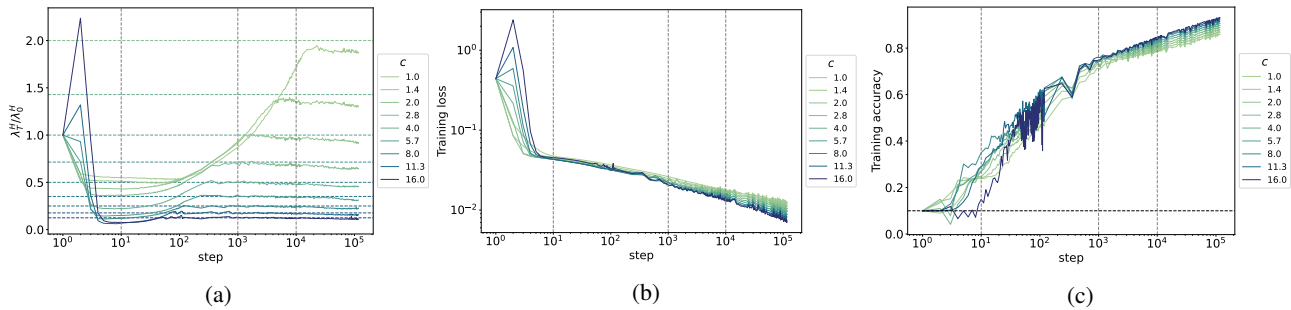


Figure 42. CNN with $d = 5$ and $w = 128$ trained on the Fashion-MNIST dataset with MSE loss using vanilla SGD for 1000 epochs with a batch size $B = 512$.

Phase diagram of training dynamics in DNNs

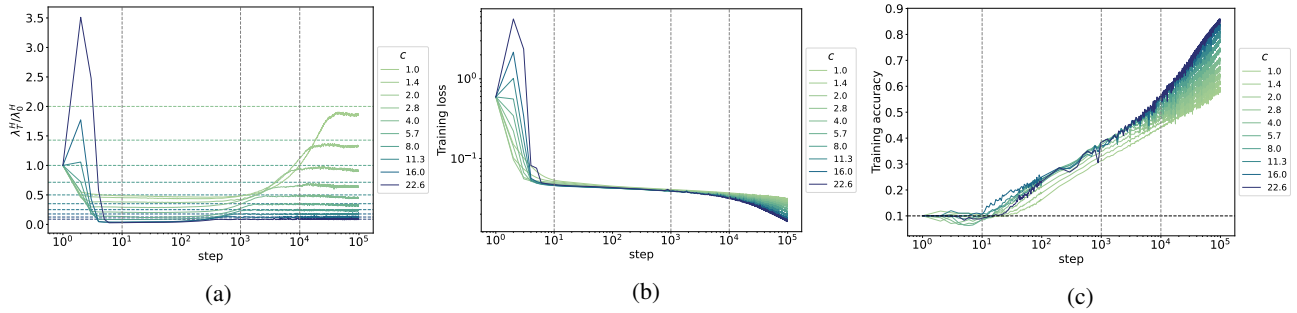


Figure 43. CNN with $d = 5$ and $w = 128$ trained on the CIFAR-10 dataset with MSE loss using vanilla SGD for 1000 epochs with a batch size $B = 512$.

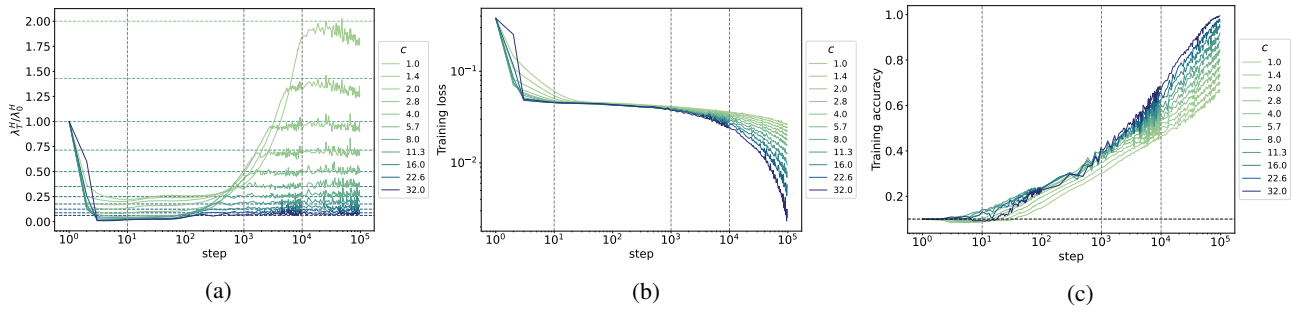


Figure 44. CNN with $d = 10$ and $w = 128$ trained on the CIFAR-10 dataset with MSE loss using vanilla SGD for 1000 epochs with a batch size $B = 512$.

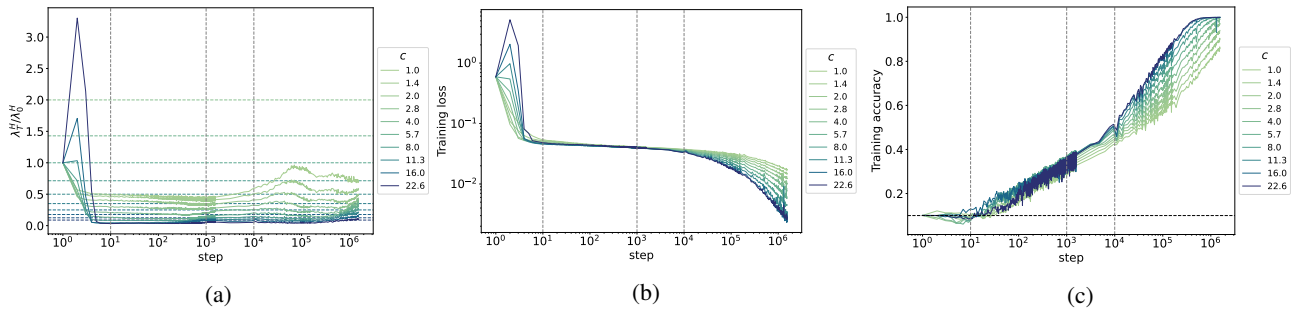


Figure 45. CNN with $d = 5$ and $w = 128$ trained on the CIFAR-10 dataset with MSE loss using vanilla SGD for 1000 epochs with a batch size $B = 32$.

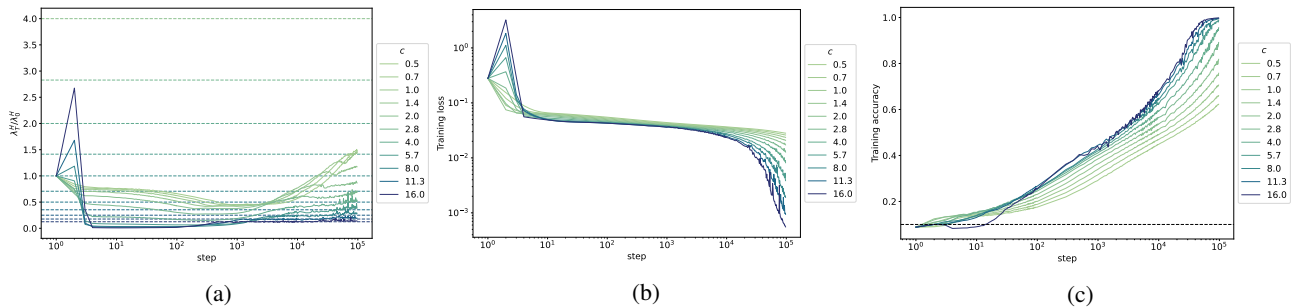


Figure 46. ResNet-18 with $w = 64$ trained on the CIFAR-10 dataset with MSE loss using vanilla SGD for 1000 epochs with a batch size $B = 512$.

Phase diagram of training dynamics in DNNs

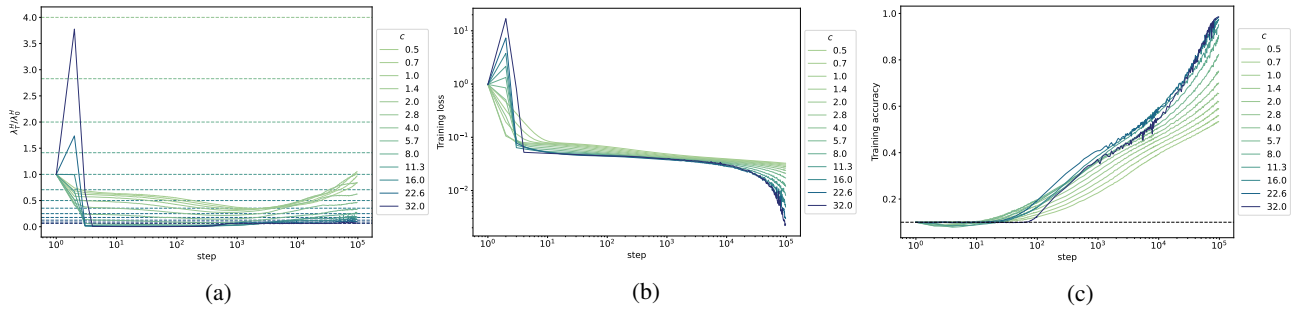


Figure 47. ResNet-34 with $w = 64$ trained on the CIFAR-10 dataset with MSE loss using vanilla SGD for 1000 epochs with a batch size $B = 512$.

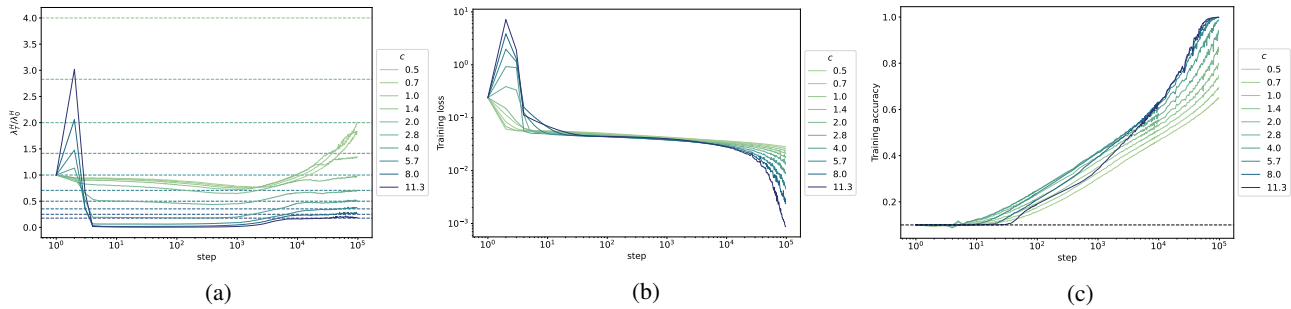


Figure 48. ResNet-50 with $w = 64$ trained on the CIFAR-10 dataset with MSE loss using SGD for 1000 epochs with a batch size $B = 512$.

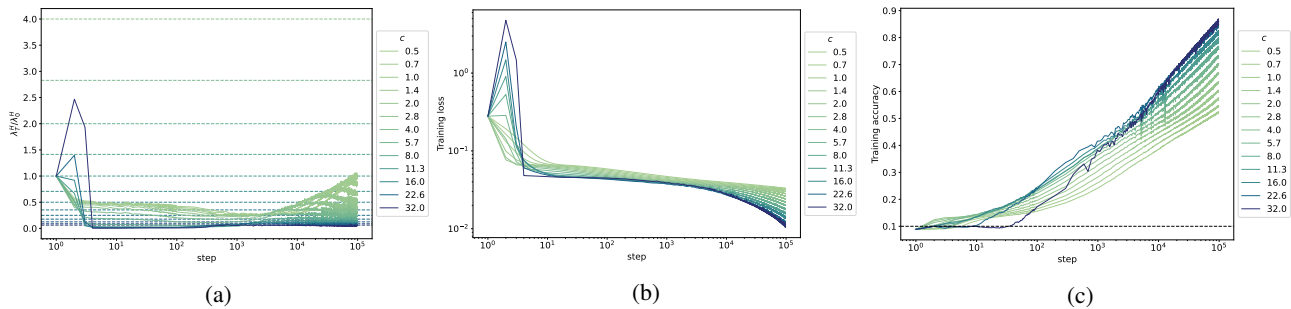


Figure 49. ResNet-18 with $w = 64$ trained on the CIFAR-10 dataset with data augmentation and MSE loss using vanilla SGD for 1000 epochs with a batch size $B = 512$.

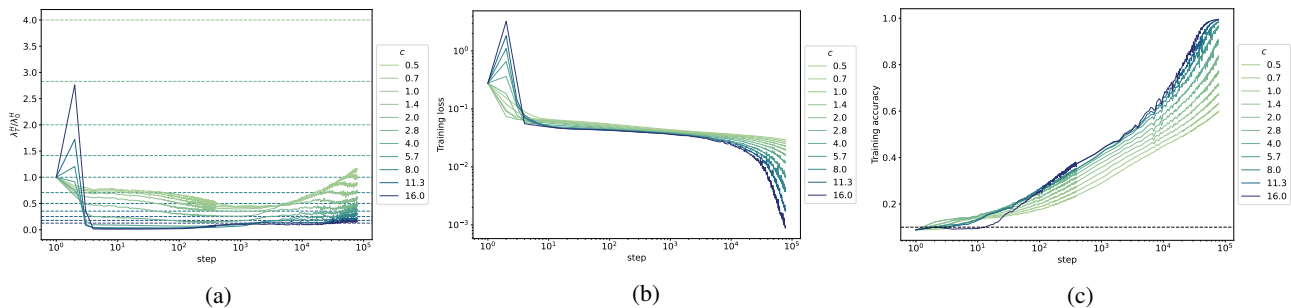


Figure 50. ResNet-18 with $w = 64$ trained on the CIFAR-10 dataset with MSE loss using vanilla SGD for 200 epochs with a batch size $B = 128$.

Phase diagram of training dynamics in DNNs

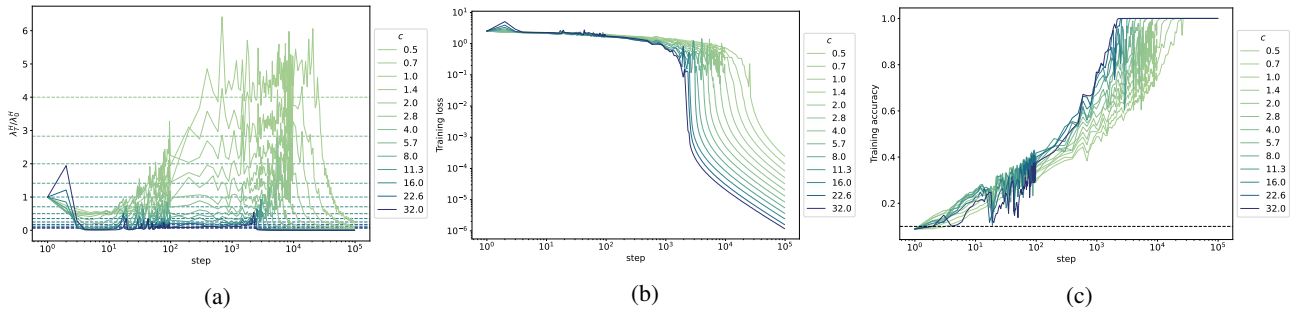


Figure 51. ResNet-18 with $w = 64$ trained on the CIFAR-10 dataset with CSE loss using vanilla SGD for 1000 epochs with a batch size $B = 512$.

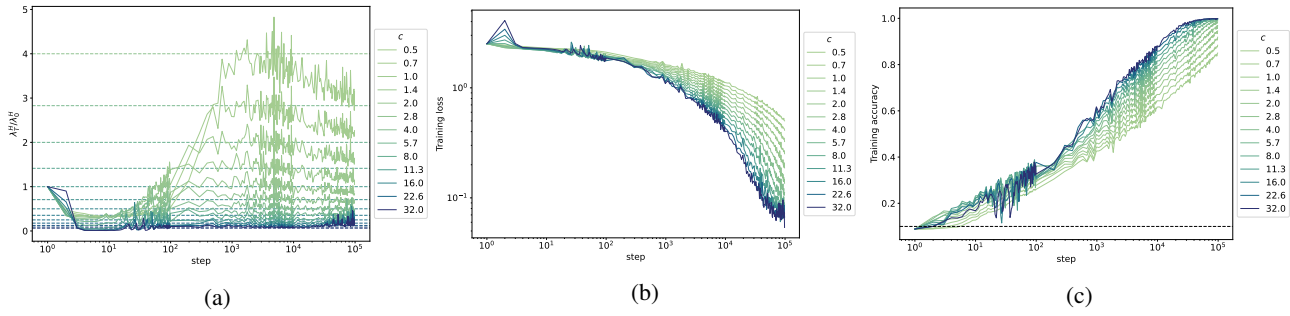


Figure 52. ResNet-18 with $w = 64$ trained on the CIFAR-10 dataset with data augmentation and with CSE loss using vanilla SGD for 1000 epochs with a batch size $B = 512$.

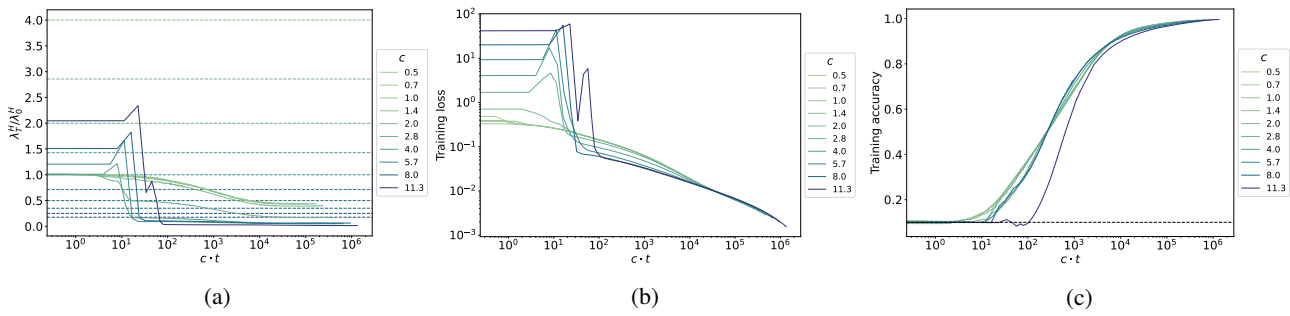


Figure 53. FCNs with $d = 4$ and $w = 2048$ trained on the MNIST dataset with MSE loss using vanilla SGD for 1000 epochs with a batch size $B = 512$.

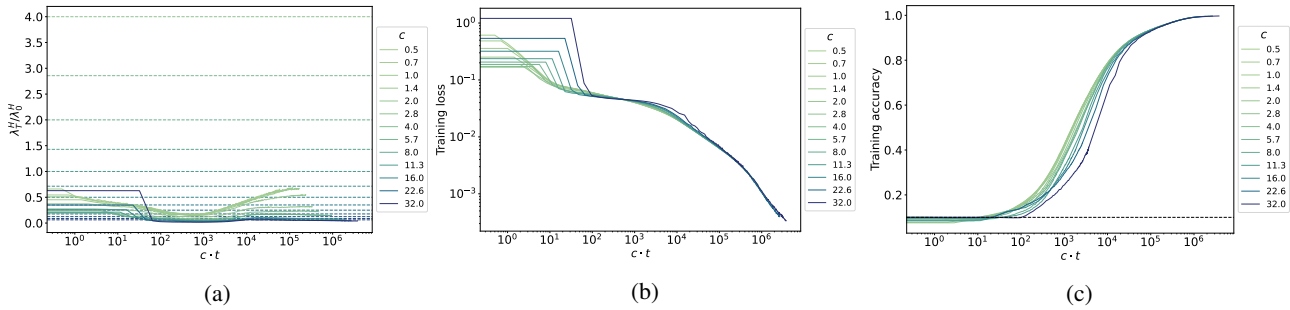


Figure 54. FCNs with $d = 16$ and $w = 256$ trained on the MNIST dataset with MSE loss using vanilla SGD for 1000 epochs with a batch size $B = 512$.

Phase diagram of training dynamics in DNNs

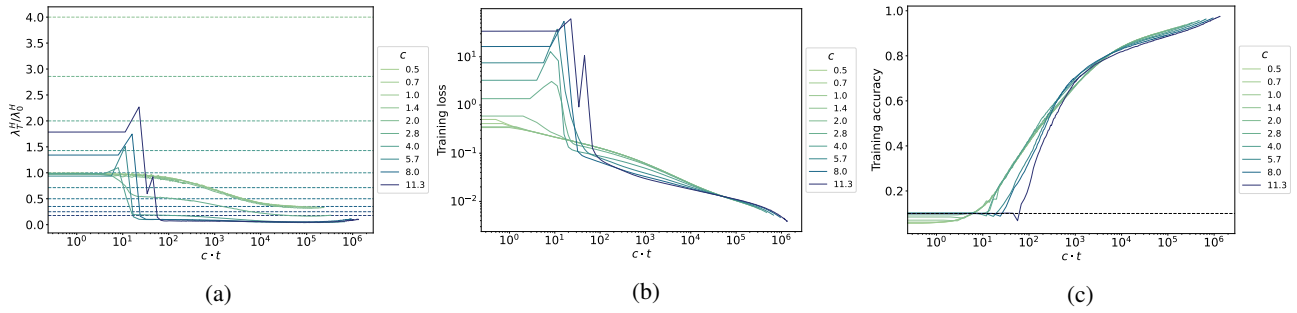


Figure 55. FCNs with $d = 4$ and $w = 2048$ trained on the Fashion-MNIST dataset with MSE loss using vanilla SGD for 1000 epochs with a batch size $B = 512$.

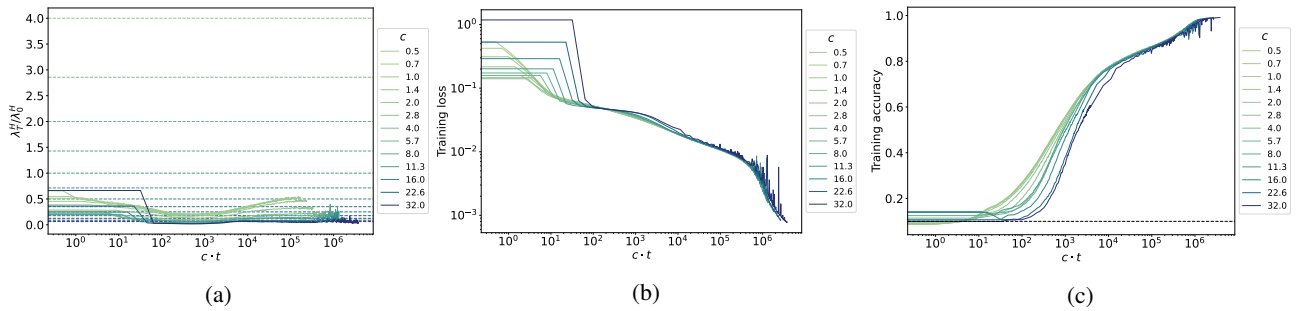


Figure 56. FCNs with $d = 16$ and $w = 256$ trained on the Fashion-MNIST dataset with MSE loss using vanilla SGD for 1000 epochs with a batch size $B = 512$.

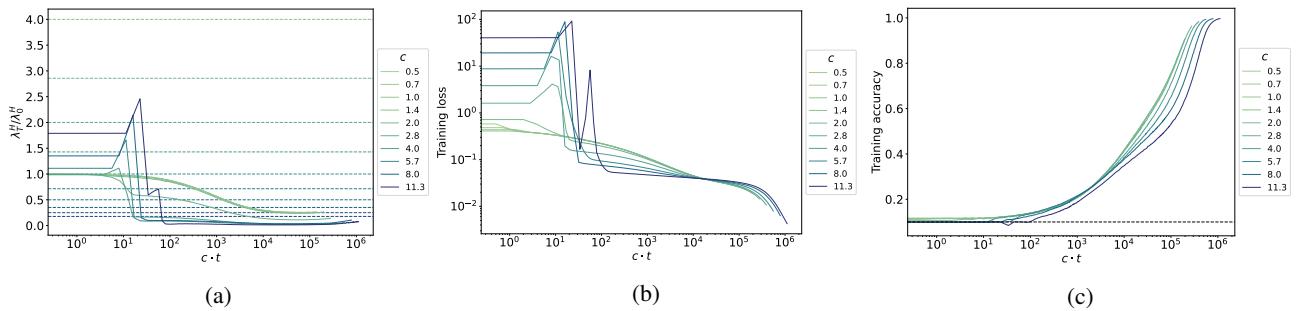


Figure 57. FCNs with $d = 4$ and $w = 2048$ trained on the CIFAR-10 dataset with MSE loss using vanilla SGD for 1000 epochs with a batch size $B = 512$.

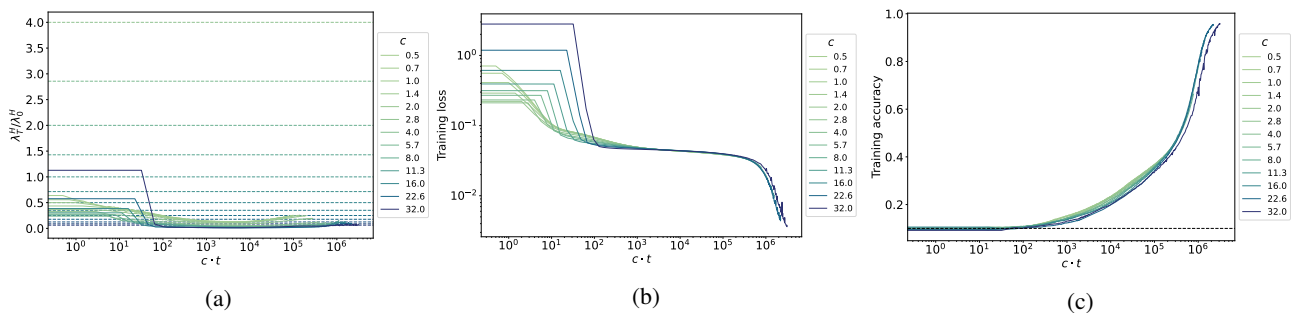


Figure 58. FCNs with $d = 16$ and $w = 256$ trained on the CIFAR-10 dataset with MSE loss using vanilla SGD for 1000 epochs with a batch size $B = 512$.

Phase diagram of training dynamics in DNNs

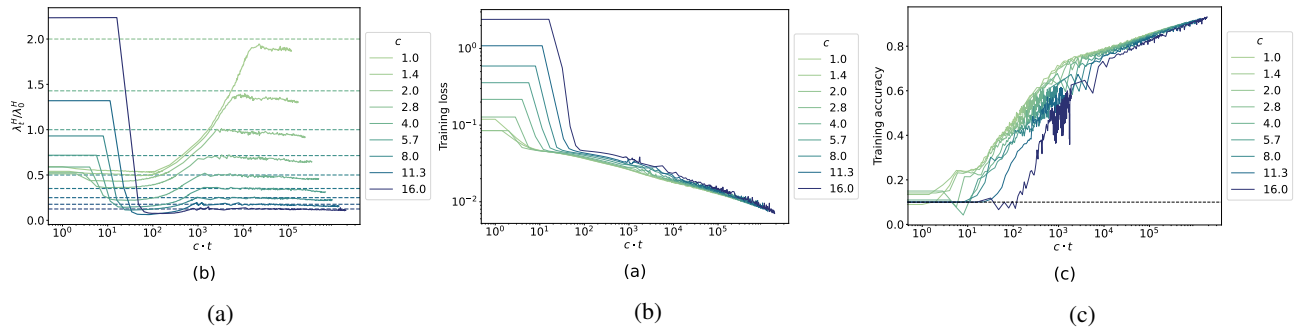


Figure 59. CNNs with $d = 5$ and $w = 128$ trained on the Fashion-MNIST dataset with MSE loss using vanilla SGD for 1000 epochs with a batch size $B = 512$.

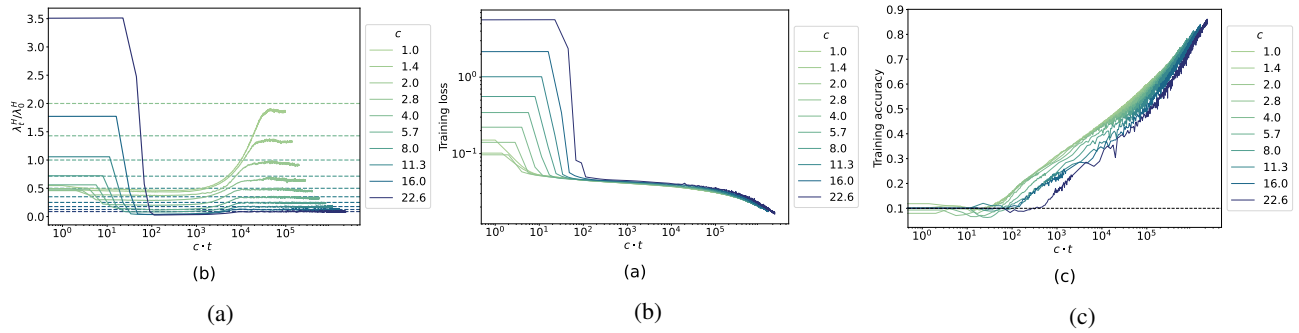


Figure 60. CNNs with $d = 5$ and $w = 128$ trained on the CIFAR-10 dataset with MSE loss using vanilla SGD for 1000 epochs with a batch size $B = 512$.

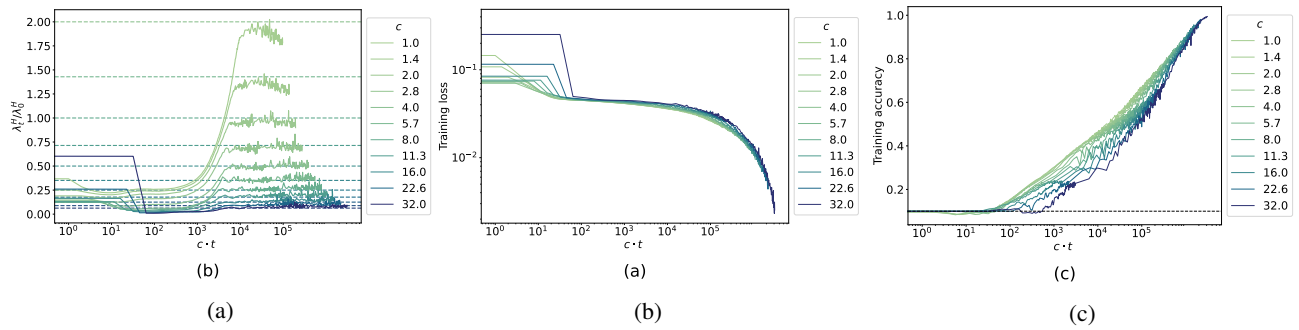


Figure 61. CNNs with $d = 10$ and $w = 128$ trained on the CIFAR-10 dataset with MSE loss using vanilla SGD for 1000 epochs with a batch size $B = 512$.

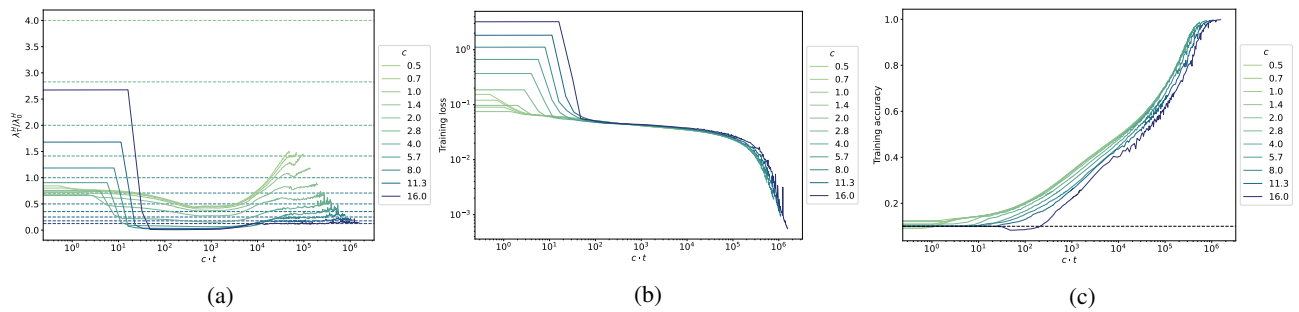


Figure 62. ResNet-18 with $w = 64$ trained on the CIFAR-10 dataset with MSE loss using vanilla SGD for 1000 epochs with a batch size $B = 512$.

Phase diagram of training dynamics in DNNs

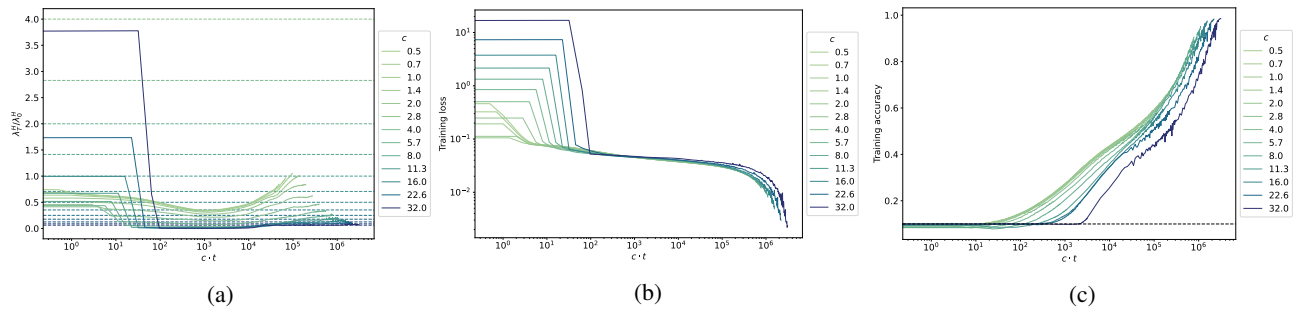


Figure 63. ResNet-34 with $w = 64$ trained on the CIFAR-10 dataset with MSE loss using vanilla SGD for 1000 epochs with a batch size $B = 512$.

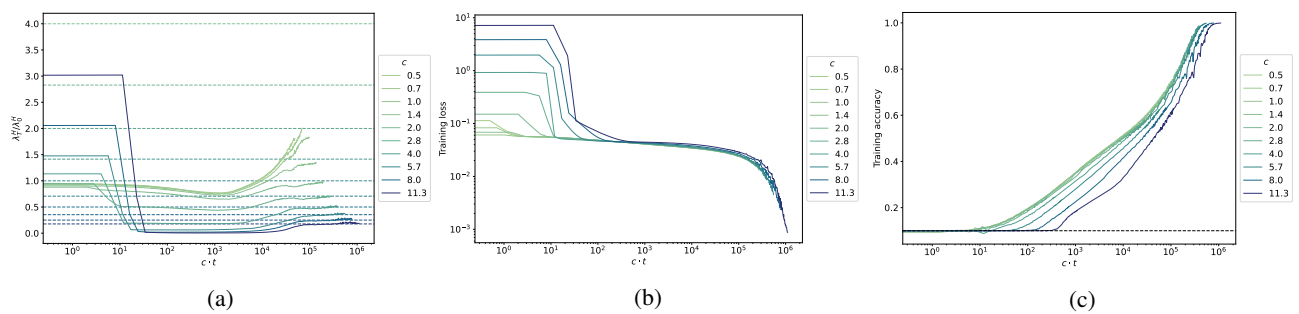


Figure 64. ResNet-50 with $w = 64$ trained on the CIFAR-10 dataset with MSE loss using vanilla SGD for 1000 epochs with a batch size $B = 512$.